scientific reports

OPEN

Photocatalytic degradation of azithromycin and ceftriaxone using synthesized Ag/g-C$_3$N$_4$/Fe$_3$O$_4$ nanocomposites in aqueous solution

Amirali Emadi Khyave[1], Roya Mafigholmi[2✉], Asghar Davood[3], Amirhossein Mahvi[4] & Lida Salimi[5]

This study focuses on the synthesis of an Ag/g-C$_3$N$_4$/Fe$_3$O$_4$ nanocomposite and its application for the photocatalytic degradation of azithromycin and ceftriaxone in aqueous solutions. The g-C$_3$N$_4$ was prepared via a two-step calcination method, while the Ag/g-C3N$_4$/Fe$_3$O$_4$ nanocomposite was synthesized using a one-step hydrothermal approach. The physicochemical properties of the nanocomposite were thoroughly characterized using XRD, FTIR, FE-SEM, TEM, and VSM. Process optimization based on the Box-Behnken Design (BBD) identified optimal conditions at pH 5.2, a catalyst dose of 0.42 g/L, reaction time of 107 min, and an initial antibiotic concentration of 10 mg/L. Under these conditions, the nanocomposite achieved degradation efficiencies of 83.3 ± 2.1% for azithromycin and 93.3 ± 1.8% for ceftriaxone. COD and TOC reductions were measured at 65.5% and 52%, respectively, although intermediate products decelerated mineralization. Catalyst reusability was demonstrated with a performance decline of less than 13% after six cycles. Additionally, light intensity and the presence of scavengers and inorganic ions were evaluated, revealing that hydroxyl radicals (OH$^•$) play a dominant role in the degradation process. The nanocomposite also exhibited enhanced visible light absorption due to its tailored bandgap and electron-hole separation efficiency. The findings confirm that the Ag/g-C$_3$N$_4$/Fe$_3$O$_4$ nanocomposite is a robust and efficient photocatalyst for antibiotic degradation, offering a sustainable and effective solution for wastewater treatment applications.

Antibiotics prevent infections in humans and animals by inhibiting or eliminating microbial development. The widespread use of antibiotics since the 1920s has led to the emergence of antibiotic resistance genes (ARG), complicating and increasing the cost of treatments[1]. Antibiotic usage, including last-resort medications, increased 39% in low- and middle-income nations and 4% in high-income countries. If antibiotic use stays the same, predicted a 15% increase in global antibiotic use[2]. The global SARSCov-2 epidemic may increase antibiotic use. Although COVID-19 is a virus, bacterial co-infections often require medications. Patients may self-medicate antibiotics without a bacterial co-infection diagnosis. Thus, the SARS-Cov-2 pandemic may boost wastewater antibiotics and preferentially favor ARG growth[3]. Ceftriaxone and azithromycin were administered to patients in Iran as part of the treatment regimen during the Corona outbreak and varying quantities of these antibiotics were detected in hospital wastewater[4]. Azithromycin is a versatile antibiotic that can inhibit the growth of a wide range of bacteria, including both Gram-positive and Gram-negative species. The antibiotic has a half-life of 2–4 days and is primarily excreted from the body through feces and urine[5]. Ceftriaxone, a

[1]Department of Environmental Sciences and Engineering, Faculty of Art and Architecture, West Tehran Branch, Islamic Azad University, Tehran, Iran. [2]Department of Environment, West Tehran Branch, Islamic Azad University, Tehran, Iran. [3]Department of Medicinal Chemistry, Faculty of Pharmaceutical Sciences, Tehran Medical Sciences, Islamic Azad University, Tehran, Iran. [4]Department of Environmental Health Engineering, Scholl of Public Health, Tehran of University of Medical Science, Tehran, Iran. [5]Department of Environmental Engineering, Faculty of Marine Science and Technology, North Tehran Branch, Islamic Azad University, Tehran, Iran. ✉email: r.mafigholami@wtiau.ac.ir

third-generation cephalosporin, is widely used for its antibacterial efficacy, lactamase tolerance, low toxicity, and minimal allergic reactions[6].

In wastewater, antibiotics penetrate the environment. Antibiotics in the environment may harm aquatic and terrestrial ecosystems. Thus, antibiotics must be removed from wastewater to prevent their release into the aquatic environment to prevent antibiotic-resistant bacteria[7]. Antibiotics are persistent pollutants that resist conventional biological treatment methods. Therefore, different technologies are needed to remove these resistant and persistent pollutants. Several methods are employed to remove persistent pollutants from aquatic environments. These include advanced oxidation processes (AOPs) like Electro-Fenton, pyrolysis, cold plasma and etc., membrane filtration, adsorption using bio-based materials, chemical precipitation, ion exchange, and electrochemical treatments[8–10]. Due to the high reactivity and limited selectivity of hydroxyl radicals (OH•), AOP_s offer great potential in these technologies. The high reactivity rate of these radicals with pollutants does not necessarily increase process efficiency[11]. AOPs have demonstrated favorable outcomes and established themselves as an effective remedy for the rapid degradation of persistent and non-biodegradable chemicals in water, such as antibiotics[12]. One of the attractive subsets of AOP_s is the photocatalysis process (PCP). Photocatalysis refers to the alteration of reaction rates or start of chemical reactions when light is present and a substance termed a photocatalyst absorbs light and participates in the chemical transformation of the reactants. A photocatalyst is a material that generates electron-hole pairs by the absorption of light and facilitates chemical reactions with the molecules it interacts with. It can recycle its chemical composition after each cycle of these interactions[13]. Photocatalysis is applied in various fields, including wastewater treatment, air purification, self-cleaning surfaces, hydrogen production, and medical applications such as inactivating microorganisms and targeting cancer cells, by harnessing light energy to drive chemical reactions[14]. PCP demonstrate superior efficiency compared to other process like biological methods in removing resistant antibiotics, offering 3–10× faster degradation rates and higher mineralization capacity. While biological processes like anaerobic digestion struggle with antibiotic toxicity, microbial inhibition, and residual metabolites, photocatalysis employs hydroxyl radicals to non-selectively degrade complex antibiotics into harmless byproducts[15]. The photocatalytic process has four phases. First, a semiconductor is excited with a specified energy to generate electron-hole pairs. Next, electron-hole couples are separated by traps that trap faster than they recombine. Following thermodynamic and kinetic restrictions, separated electrons and holes interact with adsorption substrates to cause redox reactions. The final steps include product evolution and surface regeneration[16]. The photocatalyst's oxidation or reduction power depends on its band position, not its bandgap, hence its photocatalytic degradation ability depends on it. It is commonly known that semiconductor band gaps range from 0.7 to 5 eV. The energy difference between the valance band and the conduction band of solid materials is the semiconductor band gap. An energy gap is a solid's energy range where no electron state can exist. On semiconductor band gap, several semiconductors have been used. In photocatalytic applications such water pollutant degradation, literature reports photocatalysts with band gaps of 2.0 to 3.3 eV[17]. In the last decades, various composites to develop photocatalytic materials with high adsorption, efficient electron–hole recombination, easy catalyst separation, and effective degradation of organic pollutants presented[7]. A novel photocatalytic material, graphitic carbon nitride ($g\text{-}C_3N_4$), may improve environmental remediation, water purification, and energy conversion. $g\text{-}C_3N_4$ is a graphene-like 2D polymer of carbon and nitrogen atoms. $g\text{-}C_3N_4$ is appealing for its large surface area and porosity, visible light photocatalytic efficiency, non-toxicity, environmental friendliness, thermal and chemical stability, low cost, and easy synthesis from renewable and available resources[18]. Due to its high surface area and porosity, $g\text{-}C_3N_4$ has rapid electron-hole recombination, low selectivity and specificity, and scaling problems. Researchers have combined $g\text{-}C_3N_4$ with metal nanoparticles, co-catalysts, semiconductors, carbon-based materials like graphene or carbon nanotubes, nitrogen atom doping, and functional group modification to improve its photocatalytic activity[19,20]. Fe_3O_4 is used in magnetic properties, medication delivery, and environmental remediation. Fe_3O_4 nanoparticles remove contaminants water. Magnets remove Fe_3O_4 nanoparticles from solution. Surface-group-functionalized Fe_3O_4 nanoparticles increase adsorption and catalysis. Ecosystems suffer from toxic Fe_3O_4 nanoparticles[21]. Also, the semiconductor surface can be doped with Pt, Au, and Ag to increase photocatalytic activity under light. Ag nanoparticles improve electron cavity separation, chemical stability, and photocatalytic efficiency, making them effective[22]. The $Ag/g\text{-}C_3N_4/Fe_3O_4$ composite structure enhances photocatalytic performance through distinct roles of each component and synergistic interactions. $g\text{-}C_3N_4$ as a base photocatalyst, acts as the primary light-absorbing material, generating electron-hole pairs under irradiation. Also, provides a 2D structure for efficient charge transfer and serves as a substrate for heterojunction formation. Ag nanoparticles, enhance light absorption via localized surface plasmon resonance (LSPR), broadening the spectral response into the visible range. Ag nanoparticles act as electron sinks, reducing charge recombination by trapping photogenerated electrons and provide active sites for redox reactions, improving H2 production and pollutant degradation. Fe_3O_4, introduces magnetic properties for easy catalyst recovery and forms heterojunctions with $g\text{-}C_3N_4$, aiding spatial charge separation[23]. Box-Benkin Design (BBD) optimizes engineering, science, and industry processes, goods, and systems utilizing statistical experimental design. BBD uses factorial and response surface designs. Experimental runs simulate the quadratic and interaction effects of input components on the response variable. BBD is beneficial when the input-response relationship is intricate and non-linear and the ideal input variable settings are unknown[24].

The research team have been published two study about utilization the $g\text{-}C_3N_4/Fe_3O_4/Ag$ nanocomposite catalyst to eliminate diazinon and inactivation of Escherichia coli and Bacillus subtilis bacteria in aqueous solutions. Based on the findings of these studies, the photocatalytic process has proven to be successful in specifically targeting pollutant and deactivating microorganisms[22,25].

Based on the research, this catalyst has not been utilized for the degradation of antibiotics belonging to the medicinal chemical family using a photocatalytic method, in this study, the main objectives were to synthesize an $Ag/g\text{-}C_3N_4/Fe_3O_4$ nanocomposite using the simple hydrothermal method and to characterize it through

various analytical techniques such as FESEM, EDS mapping, TEM imaging, FTIR, XRD, UV-vis, BET, and VSM analysis. Additionally, the aim was to optimize the key parameters of the photocatalysis process for the degradation of Ceftriaxone and Azithromycin antibiotics in aqueous solution. It is important to note that further research is required to validate the effectiveness of this method in treating wastewater containing these specific contaminants.

Materials and methods
Chemicals and reagents

Analytical grade ceftriaxone (CAS No: 104376-79-6, $C_{18}H_{18}N_8O_7S_3$, ≥90%), azithromycin (CAS No: 117772-70-0, $C_{38}H_{72}N_2O_{12}$.$2H_2O$, ≥95%), silver nitrate (CAS No. 7761-88-8, $AgNO_3$), melamine (CAS No. 108-78-1, $C_3H_6N_6$), ammonia (CAS No. 7664-41-7, NH_3), iron chloridetetrahydrate (CAS No. 1317-61-9, $FeCl_2.4H_2O$), Iron(III) chloride hexahydrate (CAS No. 10025-77-1, $FeCl_3·6H_2O$), urea (CAS No. 57-13-6, CH_4N_2O), ethanol (CAS No. 64-17-5, C_2H_5OH), COD vial (Low range: 0-150 mg/L), sodium hydroxide (CAS No. 1310-73-2, NaOH), sulfuric acid (CAS no. 7664-93-9, H_2SO_4), methanol (CAS no. 67-56-1, CH_3OH, HPLC grade), disodium phosphate (CAS no. 7558-79-4, DSP, Na_2HPO_4, ≥99%), potassium dihydrogen phosphate (CAS no. 7778-77-0, KH_2PO_4, ≥99%), potassium iodide (CAS no. 7681-11-0, KI, ≥99/8%), sodium thiosulfate (CAS no. 7772-98-7, $Na_2S_2O_3·5H_2O$, ≥99%), acetonitrile (CAS no. 75-05-08, CH_3CN, ≥99%), trimethylamine (CAS no. 121-44-8, $(C_2H_5)_3N$, ≥99%), benzoquinone (CAS no. 106-51-4,$C_6H_4O_2$, ≥98%), sodium nitrate (CAS no. 7631-99-4, $NaNO_3$, ≥98%), oxalic acid (CAS no. 6153-56-6, $C_2H_2O_4$, ≥98%), tert-Butanol (CAS no. 75-65-0, $(CH_3)_3COH$, ≥98%), sodium azide (CAS no. 26628-22-8, NaN_3, ≥99%) were acquired from Sigma-Aldrich, Merck, Sumchon and other Co. All compounds were utilized in analytical grade without any purification. Deionized water (16.25 MΩ/cm, Milli-Q purification system model: MILLI-Q® HX 7000 SD) was utilized for solution preparation.

Ag/g-C$_3$N$_4$/Fe$_3$O$_4$ nanocomposite

g-C$_3$N$_4$ synthesis

The g-C_3N_4 was synthesized using the two-stage direct calcination of melamine technique described in other works[26]. In a furnace (Thermo Fisher Scientific Lindberg/Blue M Box Furnace), a porcelain crucible held 6 g of melamine and 4 g of urea. The mixture was heated to 350 °C and left to react for 2 h. The mixture was then heated to 550 °C for 2 h. During synthesis, heating and cooling were maintained at 2 °C/min. After dispersing 1.0 g of g-C_3N_4 in 100 mL, 5 M HNO_3, it underwent a 24-hour reflexing reaction. The g-C_3N_4 sheets were rinsed with deionized water to neutral pH.

Ag/g-C$_3$N$_4$/Fe$_3$O$_4$ nanocomposite synthesis

A one-step hydrothermal technique produced Ag/g-C_3N_4/Fe_3O_4 nanocomposite[22]. The Fig. 1 shows the runs of Ag/g-C_3N_4/Fe_3O_4 nanocomposite synthesis. The synthesis involved the following steps:

<u>Ultrasonic dispersion</u>   50 mg of g-C_3N_4 was dispersed ultrasonically in 30 mL of deionized water for 1 h to enhance its dispersibility and expose more active sites. The ultrasonic treatment not only exfoliates the g-C_3N_4 structure but also enhances its surface area, promoting better interaction with Fe_3O_4 and Ag nanoparticles.

<u>Precursor addition and stirring</u>   0.5 g of $FeCl_2·4H_2O$, 25 mg of $AgNO_3$, and 0.1 g of PVP were added to the solution under continuous stirring for 3 h at room temperature. PVP, a stabilizing agent, was incorporated to
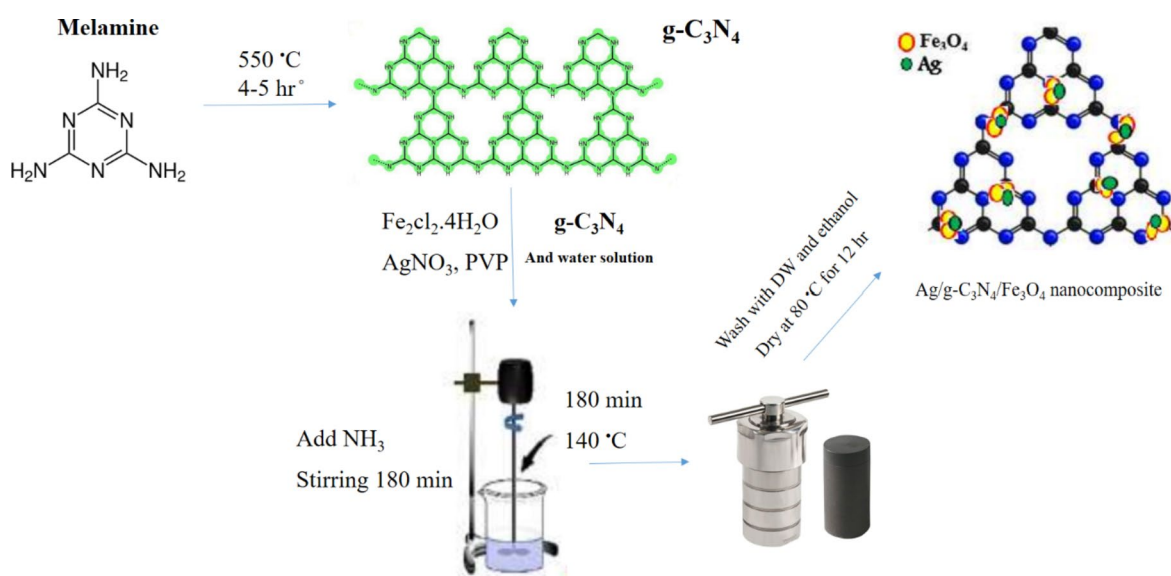

Fig. 1. Schematic synthesis of Ag/ g-C_3N_4/Fe_3O_4 nanocomposite. (Drawn with: EdrawMax Ultimate, Ver: 14.2.2.1269).

prevent nanoparticle agglomeration and facilitate uniform dispersion of Fe_3O_4 and Ag species on the g-C_3N_4 surface.

Ammonia-induced oxidation   2.5 mL of NH_3 (25 wt%) was introduced into the mixture to regulate pH and induce oxidation of Fe^{2+} to Fe^{3+} under vigorous stirring for 10 min. This step is critical for Fe_3O_4 formation, as NH_3 helps in controlling particle nucleation and growth, resulting in highly crystalline magnetic Fe_3O_4 nanoparticles.

Hydrothermal treatment   The suspension was transferred into a 50 mL Teflon-sealed autoclave and maintained at 140 °C for 3 h. The hydrothermal process ensures the strong anchoring of Fe_3O_4 and Ag nanoparticles onto the g-C_3N_4 structure, enhancing structural stability and photocatalytic properties.

Washing and drying   The synthesized material was collected, washed multiple times with deionized water and ethanol at 80 °C to remove unreacted precursors and stabilizing agents. The purified sample was dried at 80 °C for 12 h to ensure the complete removal of residual solvents.

Preparation of g-C_3N_4/Fe_3O_4 (without Ag)   To further analyze the impact of Ag incorporation, a two-component g-C_3N_4/Fe_3O_4 composite was synthesized using the same method but without the addition of $AgNO_3$.

Characterization

The surface morphology of the g-C_3N_4, g-C_3N_4/Fe_3O_4, and Ag/g-C_3N_4/Fe_3O_4 nanocomposite was analyzed using a field-emission scanning electron microscope (FE-SEM, [SEM4000X, CIQTEK]). The measurements were conducted under high vacuum conditions, maintaining a minimum pressure of $\leq 1.3 \times 10^{-4}$ mbar to ensure high-resolution imaging. Secondary electron (SE) and backscattered electron (BSE) modes were utilized to capture detailed morphological and compositional contrast. The accelerating voltage was set at [5–20 kV] based on the sample's conductivity. To complement the morphological analysis, energy-dispersive X-ray spectroscopy (EDS) and elemental mapping were performed to confirm the elemental composition and distribution, ensuring the chemical purity and homogeneity of the synthesized nanocomposites. Transmission electron microscopy (TEM) analysis was carried out using a [JEM-ACE200F, Jeol] with an accelerating voltage of 200 kV. The samples were prepared by dispersing the nanocomposites in ethanol and drop-casting onto carbon-coated copper grids, followed by air-drying.

Fourier-transform infrared (FT-IR) spectroscopy was employed to identify the functional groups present in the as-synthesized nanomaterials. The spectra were recorded using an FT-IR spectrometer ([Frontier, PerkinElmer]) in the range of 4000–400 cm^{-1} with a resolution of 4 cm^{-1}. The samples were prepared using the KBr pellet method to ensure optimal infrared transmittance.

X-ray diffraction (XRD) patterns were produced using the XRD diffractometer Rigaku-ZSX Primus 400. The radiation source employed was a monochromatic incident beam of Cu Kα ($\lambda = 1.54056$ Å), spanning from 10° to 80° with a step interval of 0.02° and a rate of 0.05 °/s. The recorded patterns were used to assess the crystal structure of the structures. In addition, the average size of the crystals (D) in the nanocomposite can be determined using the Debye-Scherrer equation (Eq. (1))[27].

$$D = \frac{0.9\,\lambda}{\beta\,cos\theta} \tag{1}$$

Where, D represents the size of the crystallite, λ refers to the wavelength of X-rays, β represents the full width at half maximum (FWHM) of the diffraction peak, and θ indicates the Bragg angle. The FWHM is a quantitative measure of the extent of the diffraction peak, specifically the breadth between the points when the intensity drops to half of its greatest value.

Ultraviolet-visible (UV-Vis) spectroscopy was conducted to evaluate the optical properties of the synthesized materials. The absorption spectra were recorded using a [UV-3600 Plus, Shimadzu] in the wavelength range of [Specify Range, e.g., 200–800 nm]. The bandgap energy of the samples was estimated using the Tauc plot method (Eq. (2))[28].

$$\left(\alpha' h\upsilon\right)^2 = A\left(h\upsilon - E_g\right) \tag{2}$$

Where, the symbol ὰ represents the absorption coefficient, h represents Planck's constant, v represents the frequency of the light, A represents a constant that is connected to the material parameters, and Eg represents the bandgap energy of the material.

To assess the specific surface area and porosity of the nanocomposites, nitrogen adsorption-desorption isotherms were obtained using the Brunauer-Emmett-Teller (BET) method. The measurements were performed on a [TriStar II Plus, Micromeritics] at liquid nitrogen temperature (77 K). The specific surface area was determined using the BET equation, while the pore size distribution was analyzed via the Barrett-Joyner-Halenda (BJH) method.

Point of zero charge measurements of Ag/g-C_3N_4/Fe_3O_4 nanocomposite

The potential of zero charges (pH_{pzc}) of the Ag/g-C_3N_4/Fe_3O_4 nanocomposite was determined using the pH drift method[7]. The pH_{pzc} of Ag/g-C_3N_4/Fe_3O_4 nanocomposite was measured in six Erlenmeyer flasks. The flasks held 25 mL of distilled water with pH values from 2 to 12. After adding 0.1 g of nanocomposite to each flask, pH levels were tested again after 24 h.

Experiments set-up

Performance evaluation of the produced nanocomposite with ceftriaxone and azithromycin as the target pollutants. Tests were conducted at 25 ± 2 °C and ambient pressure. A horizontal rectangular photocatalytic reactor (15cmx8cmx5cm) with a volumetric and usable capacity of 600 and 500 mL was used in this study. The intensity of visible light, UV-C (254 nm), and UV-A (365 nm) were examined. An inner reactor quartz sheath held the light source without any distance between the source light and sample. The reactor was enclosed in a PVC box to regulate light emission. Stock solutions (100 mg/L) were prepared by dissolving antibiotics powder. Different concentrations were then prepared from this stock solution. The pH levels of the samples were adjusted by precisely adding H_2SO_4 and NaOH (0.1 N). The pH of the solutions was later determined and modified using a pH meter (HI-110 - Canada). The laboratory digital scale was used to measure various quantities of nanocomposite. The nanocomposite was added when the sample preparation was completed, and then the procedure began. Uniform blending within the reactor was achieved by utilizing mechanical agitation. After each stage, samples were taken and the nanocomposite centrifuged out. Next, antibiotics concentration was measured using high-performance liquid chromatography. The antibiotics removal performance was determined by (Eq. (3))[29].

$$\text{Efficiency } (\%) = \frac{(C0 - Ce)}{C0} \times 100 \tag{3}$$

Where, C_0 and C_e are the initial and final concentrations (mg/L) of antibiotics.

Optimize study variables via BBD

The BBD evaluated the effects of pH, catalyst dosage, reaction time, and initial antibiotic concentration on photocatalytic efficiency, with defined high and low ranges (Table 1). The selection of parameter ranges was based on preliminary experiments and literature review to ensure effective degradation performance while maintaining practical applicability. The pH range (4–8) was chosen based on the known influence of acidity and alkalinity on the charge state of the photocatalyst and the target pollutant. The catalyst dosage (0.25–0.5 mg/L) was selected to balance photocatalytic activity and light penetration without excessive agglomeration. The antibiotic concentration (10–20 mg/L) reflects typical contamination levels in wastewater treatment scenarios. The reaction time (60–120 min) was set based on prior kinetic studies indicating that most degradation occurs within this timeframe.

Empirically, a second-order polynomial model was developed to represent the elimination of antibiotics in the PCP, as described in (Eq. (4))[7].

$$Y = \beta_0 + \sum_{i=1}^{k} \beta_i x_i + \sum_{i=1}^{k} \beta_{ii} x_i^2 + \sum_{i=1}^{k-1} \sum_{j=i+1}^{k} \beta_{ij} x_i x_j + \varepsilon \tag{4}$$

Y (%) represents the removal of antibiotics (%) and has an intercept b_0 and coefficients i, i_i, and i_j for the linear, quadratic, and interaction effects of x_i and x_j, experimental levels. Coded values were derived using (Eq. (5)) for the comparison of factors with different units.

$$x_i = \frac{X_i - X_0}{\Delta x} \tag{5}$$

The data comprises encoded values of xi, the disparity between high and median values of x, actual variable values, and median values of X_0. The statistical significance of the model and the interaction between the response (antibiotic removal efficiency) and independent variables were assessed using analysis of variance (ANOVA). The ANOVA results included F-values and p-values to evaluate the effect of individual factors and their interactions. A low p-value (< 0.05) indicated a significant effect of the corresponding factor.

The model's goodness-of-fit was evaluated using correlation coefficients, including. R^2, which indicates the proportion of variance explained by the model. Adjusted R^2, which corrects R^2 for the number of predictors to prevent overfitting. Predicted R^2, which measures the model's predictive ability for new data points. The lack-of-fit test was performed to determine whether the model adequately represents the experimental data. A non-significant lack-of-fit ($p > 0.05$) suggests a well-fitted model, whereas a significant lack-of-fit indicates potential inadequacies in capturing response variations[7].

Factors	Names	Units.	Min	Max	Coded low	Coded high	Mean	Std. dev.
A	pH of solution	-	4	8	−1 ↔ 4	+1 ↔ 8	6	1.82
B	Catalyst dose	mg/L	0.25	0.5	−1 ↔ 10	+1 ↔ 20	0.375	0.08
C	Antibiotics Concentration	mg/L	10	20	−1 ↔ 10	+1 ↔ 20	15	3.27
D	Reaction time	min	60	120	−1 ↔ 60	+1 ↔ 120	90	19.6

Table 1. The values of variables in BBD.

Supplementary studies

Kinetic of reaction
Under optimal process conditions, it was established that the antibiotic removal rate adheres to a first-order reaction (Eq. (6))[30].

$$In\left(\frac{Ct}{C0}\right) = -Kt \qquad (6)$$

Where C_0, C_t, t, k_{app} represents the initial and residual concentration of antibiotics (mg/L), the reaction time (min), and is the rate constant (1/min) respectively.

Synergistic impact of mechanisms
An evaluation was conducted to ascertain the combined impact of various treatment processes, including photolysis, sorption, and PCP, under optimum circumstances. The synergistic impact as ascertained by (Eq. (7))[30].

$$\text{Synergist impact } = \frac{Performance\ of\ PCP\ process\ (\%)}{Sum\ of\ adsorption\ and\ photolysis\ (\%)} \qquad (7)$$

Durability and reusability of photocatalyst
The durability and reusability of the Ag/g-C$_3$N$_4$/Fe$_3$O$_4$ nanocomposite in the PCP to antibiotics removal was evaluated by a series of five experiments that were successfully carried out in succession.

Organic and inorganic scavengers effect
The reactivity of reactive oxygen species (ROS) with radical scavengers such as methanol, tert-butanol (TBA), KI, benzoquinone (BQ), and sodium azide (SA) was explored at the optimal condition of PCP. Additionally, the effect of the presence of anions such as PO_4^{3-}, NO_3^-, CO_3^{2-}, Cl^-, and SO_4^{2-} was also investigated.

Energy efficiency
Based on (Eq. (8)), the EE/O of the PCP in the optimal condition was calculated[31].

$$EE/O = \frac{Pelec \times t \times 1000}{V \times 60 \times \log\left(\frac{C0}{Ct}\right)} \qquad (8)$$

Where, EE/O (kW/h-m^3-order^1), P_{elec} (kW), t(min), V(L), C_0 (mg/L), and C_t(mg/L) are the electrical energy per order, the rate power, the reaction time, the volume of reactor, and the initial and final of antibiotics concentration.

Adsorption capacity and impact of catalyst components
The impact of catalyst components individually (g-C$_3$N$_4$, /Fe$_3$O$_4$, g-C$_3$N$_4$/Fe$_3$O$_4$, Ag/g-C$_3$N$_4$/Fe$_3$O$_4$) on the removal of antibiotics was examined at optimal PCP conditions. The adsorption capacity of g-C$_3$N$_4$, /Fe$_3$O$_4$, g-C$_3$N$_4$/Fe$_3$O$_4$, Ag/g-C$_3$N$_4$/Fe$_3$O$_4$ was assessed according to (Eq. (9))[32].

$$Adsorption\ capacity\ (q) = \frac{(C0 - Ce) \times V}{M} \qquad (9)$$

Where, q represents the adsorption capacity (mg/g), C_0 and C_e the beginning and final concentrations of antibiotics in the solution (mg/L), V, the volume of the solution (L), and M, the mass of the adsorbent (g).

Light intensity impact and light sources
The impact of light intensity on PCP on the removal of antibiotics was examined under optimal conditions. Three Xenon lights, each with a power output of 15 watts, were utilized for this purpose. The light intensity can be determined using (Eq. (10))[33].

$$I = \frac{P}{A} \qquad (10)$$

Where, I, the light intensity (W/m^2), P, the power of the light source (W), A, the surface area of the reactor (m^2).
  The impact of several light sources, including UV-C (GE 15870 F9W/T5/2P/SE/30 UV-C Lamp, 254 nm, 9 W), UV-A (Philips Actinic BL TL-D 18 W/10 UV-A Lamp, 365 nm, 9 W), and visible light (Philips Master PL-C 26 W/840 Visible Light Lamp, Xenon, 26 W), was examined under optimal conditions. Since the lamps emitted a single wavelength, the use of a cutoff filter was unnecessary. Additionally, the lamp's intensity, as specified by the manufacturer, was deemed sufficient for the study.

Mineralization tests
COD, and TOC tests can be employed to evaluate the advancement of the PCP reaction and determine the efficacy of the photocatalyst. A reduction in COD and TOC signifies the mineralization of organic molecules and the transformation of organic carbon into carbon dioxide. The COD and TOC were assessed under optimal conditions of the PCP. The intermediates and by-products produced during the PCP of antibiotics degradation at optimal conditions were identified using gas chromatography-mass spectrometry (GC-MS).

Analytical methods

Azithromycin and ceftriaxone concentrations were measured using an HPLC system with a UV-visible detector and an Agilent Technologies Zorbax SB-C18 C18 column. HPLC was used to measure antibiotic concentration using a Shimadzu LC-20 AB pump (140 mm×260 mm×420 mm, T: 4–35 °C, max discharge pressure: 40 MPa, flow rate range: 0.0001–10 mL/min, solvent delivery method: parallel-type double plunger, plunger capacity: 10 μL) and a C18 column (250 mm×4.6 mm, 5 μm particle size, 12 nm pore size, surface area: 410 m^2/g, carbon loading: 20%, pore volume: 1.25 mL/g). The mobile phase to the azithromycin detection was formulated by combining Methanol and Phosphate buffer in a 9:1 (v/v) ratio, with a flow rate of 1.5 ml/min, utilizing a UV detector set to 210 nm, and a column oven temperature of 40° C, with an injection volume of 20 μL[34]. Also, the mobile phase to ceftriaxone detection was comprised acetonitrile and water in a 70:30 (v/v) ratio. The pH of the mobile phase was adjusted to 6.5 using 0.01% triethylamine. The flow rate was maintained at 1.5 ml/min, and the column was configured at ambient temperature. Eluents were monitored via a UV detector at 270.0 nm[35]. The limits of detection and quantification (LOD and LOQ) were calculated using the standard deviation of the response and the slope of the calibration curves. GC (Agilent 7890 A and Agilent 5975 C, California, USA)-MS (Agilent 5975 C) system via DB-5MS column (30 m 0.25 mm 0.5 lm film thickness) and high-purity helium (99.99%) was utilized to analyze the degradation of the intermediates. The column temperature was originally set at 35 °C for one min, then increased to 300 °C at a rate of 7.0 °C/min, and held for one min. A 10 μL injection of the sample was performed, with both the injector and detector calibrated to a temperature of 280 ºC[7]. TOC was quantified utilizing a Multi Total Organic Carbon Analyzer (2100, Analytik Jena AG Corporation). The Chemical Oxygen Demand (COD) was quantified using the closed reflux method (No. 5220 D, colorimetric method) via a UV–Visible spectrophotometer (DR 6000, HACH, USA), as outlined in standard methodologies for water and wastewater analysis[7].

Results and discussion

Characterization of pure g-C$_3$N$_4$, g-C$_3$N$_4$/Fe$_3$O$_4$ and Ag/ g-C$_3$N$_4$/Fe$_3$O$_4$ nanocomposite

FT-IR

An investigation was performed using FT-IR analysis to identify the functional groups on the surface of the specimens within the spectral region of 4000–500 cm-1, as illustrated in Fig. 2.

According to Fig. 2, the synthesized g-C$_3$N$_4$ exhibited strong spectral bands in the 1100–1750 cm^{-1} region. The prominent peaks seen at roughly 1240, 1320, 1413, and 1465 cm^{-1} correspond to the vibrations of aromatic C–N stretching. The C = N stretching vibrations were focused at 1572 and 1652 cm^{-1}. The unique and isolated signal observed at 810 cm^{-1} was attributed to the vibrational mode of s-triazine compounds. The spectral range of 3075–3325 cm^{-1} was attributed to the stretching of N–H and O–H bonds, resulting from the adsorption of H$_2$O. The FTIR spectra of the g-C$_3$N$_4$/Fe$_3$O$_4$ exhibit, in addition to the peaks characteristic of pure g-C$_3$N$_4$, a distinct broad Fe–O band within the range of 550 to 650 cm^{-1}. The peaks at 1243 and 1637 cm^{-1} correspond to C-N and C = C stretching vibrations, respectively, whereas the peak at 808 cm^{-1} is associated with s-triazine ring vibrations. The OH stretching vibrations of adsorbed water molecules are detectable as a broad band between
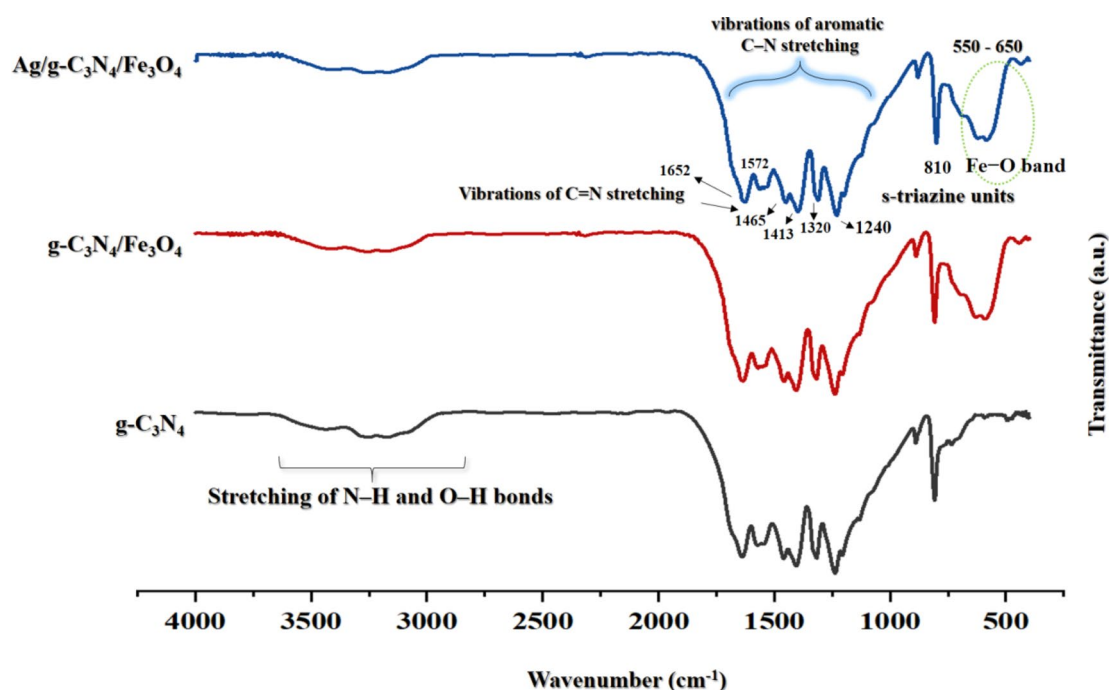

Fig. 2. FT-IR spectra of pure g-C$_3$N$_4$ and g-C$_3$N$_4$/Fe$_3$O$_4$ and Ag/ g-C$_3$N$_4$/Fe$_3$O$_4$ nanocomposite (Drawn with: Origin Pro, Ver: 10.1.0.178).

3300 and 3600 cm^{-1} and a distinct band at 1658 cm^{-1}. Finally, the results presented for the FTER spectrum of the g-C$_3$N$_4$/Fe$_3$O$_4$ nanocomposite indicate that the spectra are identical in the structure of Ag/ g-C$_3$N$_4$/Fe$_3$O$_4$ nanocomposite and Ag/ g-C$_3$N$_4$/Fe$_3$O$_4$ nanocomposite. In the study of Ghodsi et al., Pure g-C3N4 has a broad FT-IR band from 3000 to 3400 due to (NH) and (-NH$_2$) stretching vibrational modes. C-N and C=N bonds are associated with the peaks at 1251, 1325, 1419, 1463, 1575, and 1639 cm^{-1}. The peak at 808 cm^{-1} is connected to s-triazine unit bending vibration, and a large Fe-O band developed between 430 and 650 cm^{-1}[122].

XRD

XRD analysis was utilized to ascertain the crystalline characteristics of pure g-C$_3$N$_4$, g-C$_3$N$_4$/Fe$_3$O$_4$ and Ag/ g-C$_3$N$_4$/Fe$_3$O$_4$ nanocomposite Fig. 3. Findings indicate that g-C$_3$N$_4$ has a prominent peak at 2θ = 27.5°, which corresponds to the distinctive interplanar stacking peak (002) of an aromatic system, associated with the tri-S-triazine unit as per JCPDS file No. 87-1526[36,37]. In Ag/g-C$_3$N$_4$/Fe$_3$O$_4$ nanocomposite, alongside the peak associated with g-C$_3$N$_4$, additional peaks have emerged at 2θ values of 30.1°, 53.4°, 57.0°, and 62.6°, corresponding to the (220), (311), (400), (422), (511), and (440) planes, which can be attributed to Fe$_3$O$_4$ (JCPDS: 85-1436). The peaks at 35.5° and 43.1°, correspond to the planes (111) and (200), respectively, showing the presence of Ag. The intensity of the g-C$_3$N$_4$ peak in the nanocomposite diminished relative to that of pure g-C$_3$N$_4$, attributable to the lower accumulation of g-C$_3$N$_4$ and the incorporation of Fe$_3$O$_4$ and Ag within the nanocomposite framework[22]. Reducing the intensity of the g-C$_3$N$_4$ peak can help improve the photocatalytic properties of the nanocomposite, as it increases the contact area and interfacial interactions. To further validate the crystalline structure, the Scherrer equation (Eq. 1) was employed to estimate the average crystallite size of the Ag/g-C$_3$N$_4$/Fe$_3$O$_4$ nanocomposite, yielding a value of 369 Å. The reduction in peak intensity and broadening of diffraction peaks suggest a reduction in crystallite size and possible lattice strain, which could influence the material's catalytic and magnetic properties. Furthermore, the slight shifts in diffraction angles and peak broadening in the synthesized nanocomposite suggest strong interactions between the constituent phases, likely due to the formation of Fe-O-C or Ag-N bonds. Such interactions could enhance the structural stability and functionality of the nanocomposite in catalytic or magnetic applications. Additionally, the absence of impurity peaks confirms the high purity of the synthesized material, further corroborating the successful incorporation of Fe$_3$O$_4$ and Ag within the g-C$_3$N$_4$ matrix. In a study conducted by Ghodsi and coworkers, XRD investigations were performed within the 2θ range of 20–80°. A significant peak at 27.6° was observed for pure g-C$_3$N$_4$, which corresponds to the (002) plane of an aromatic compound. The nanocomposite's peaks were detected at 30.2°, 35.8°, 43.5°, 53.7°, 57.3°, and 62.7°, matching the (220), (311), (400), (422), (511), and (440) planes, respectively. These peaks correspond to the Fe3O4 phase and are consistent with previous studies[25].

FESEM, EDS, elemental mapping, and TEM

The morphology of the pure g-C$_3$N$_4$ and Ag/g-C$_3$N$_4$/Fe$_3$O$_4$ nanocomposite analyzed by the use of FESEM Fig. 4. Pure g-C$_3$N$_4$ displayed a surface that was both smooth and irregular plane structure (Fig. 4a). Also, Fig. 4b, illustrates the morphology of the Ag/ g-C$_3$N$_4$/Fe$_3$O$_4$ nanocomposite. This result illustrates the successful deposition of Fe$_3$O$_4$ nanoparticles and Ag onto the surface of g-C$_3$N$_4$ sheets. Certain void formations have arisen due to the partial connection and overlapping of the curved sheets. Furthermore, the minute crystalline dimensions of Fe$_3$O$_4$ nanoparticles and their tendency to agglomerate complicate the visualization of Fe$_3$O$_4$ particles in the FESEM image. The TEM image (Fig. 4c) revealed a core-shell structure in the Ag/g-C$_3$N$_4$/Fe$_3$O$_4$ nanocomposite. The g-C$_3$N$_4$ has a sheet-like structure, while Fe$_3$O$_4$ exhibits a cubic form. The in-situ growth mechanism has been effective in depositing Fe$_3$O$_4$ nanoparticles and Ag onto the surface of the g-C$_3$N$_4$ sheets. The occurrence of free Fe$_3$O$_4$ nanoparticles outside the g-C$_3$N$_4$ sheets was minimal, which significantly reduces the risk of agglomeration of the Fe$_3$O$_4$ nanoparticles. The
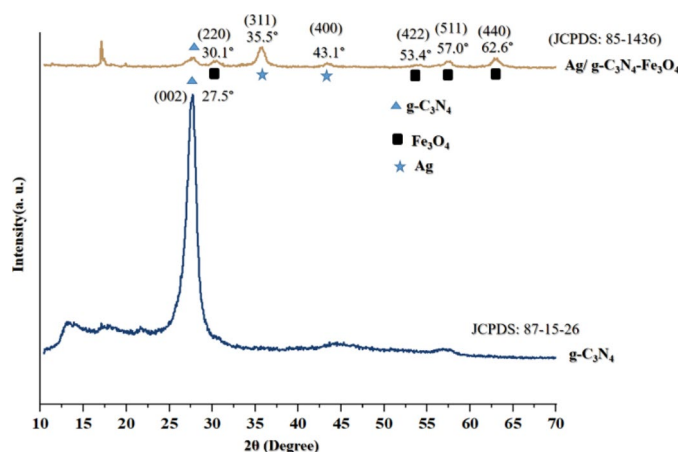

Fig. 3. XRD pattern of pure g-C$_3$N$_4$ and Ag/g-C$_3$N$_4$/Fe$_3$O$_4$ nanocomposite (Drawn with: Origin Pro, Ver: 10.1.0.178).
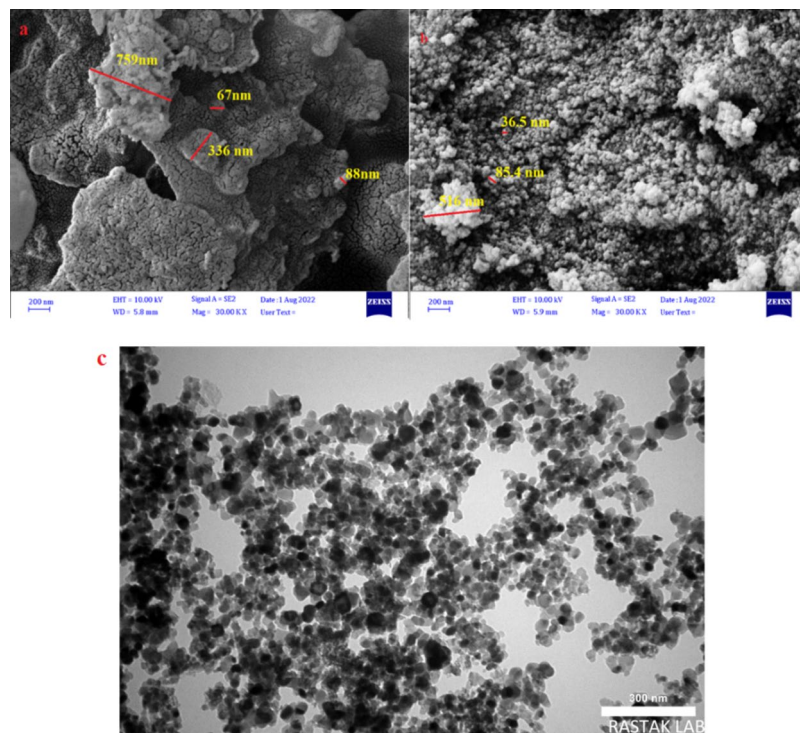
Fig. 4. FESEM, and TEM analysis of pure g-C$_3$N$_4$ and Ag/g-C$_3$N$_4$/Fe$_3$O$_4$ nanocomposite.

Element	Number	Mass[%]	Atom [%]
Fe	26	44.97	17.78
O	8	20.13	33.66
C	6	13.34	29.18
N	7	11.17	13.51
Ag	47	9.64	5.32
Cl	17	0.75	0.54
		100	100
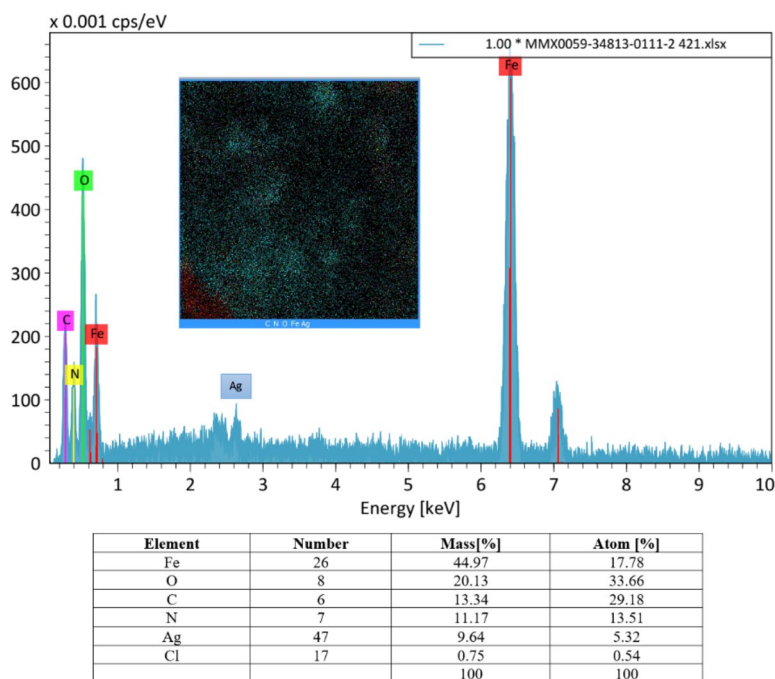
Fig. 5. EDS and elemental mapping of Ag/ g-C$_3$N$_4$/Fe$_3$O$_4$ nanocomposite (Drawn with: Origin Pro, Ver: 10.1.0.178).

size of the Fe$_3$O$_4$ nanoparticles was measured to be approximately 22 nm. Kumar and colleagues reported comparable findings in their study[38].

The (Fig. 5) illustrated Ag/g-C$_3$N$_4$/Fe$_3$O$_4$ EDS and elemental mapping analysis. Based on findings, the composite consists of carbon (13.34 W%) and nitrogen (11.17 W%), iron (44.96 W%), silver (9.64 W%) and oxygen (20.13 W%) elements. In Zhu and coworkers' study through EDX spectroscopy analysis of

the Fe_3O_4 nanoclusters in the $Ag/Fe_3O_4/g$-C_3N_4 sample, the elements Fe, O, Ag, C, and N were clearly identified. This finding indicates that the Ag species preferentially deposits on the surface of Fe_3O_4[39].

VSM, BET, and UV-vis spectra

The magnetic properties of pure Fe_3O_4 and the Ag/g-C_3N_4/Fe_3O_4 nanocomposite were examined (Fig. 6a). The saturation magnetizations were found to be 31/12 emu/g for pure Fe_3O_4 and 8/62 emu/g for the Ag/g-C_3N_4/Fe_3O_4 nanocomposite, respectively. The Ag/g-C_3N_4/Fe_3O_4 nanocomposite exhibited a lower saturation magnetization than pure Fe_3O_4, however it was sufficiently robust to facilitate collection from aqueous solutions. Prior research has noted a reduction in the magnetic properties of nanocomposite materials consisting of pure Fe_3O_4. For instance, the work of Habibi-Yangjeh reported VSM measurements of pure Fe_3O_4 and g-C_3N_4/Fe_3O_4 anchored with $CoMoO_4$ nanoparticles as 55/4 and 20/1 emu/g, respectively[40].

The diffuse reflectance spectra (270–720 nm) for pure g-C_3N_4 and Ag/g-C_3N_4/Fe_3O_4 are presented in (Fig. 6b). The optical absorption edge (OAE) of g-C_3N_4 typically appears between 400 and 500 nm in the UV-Vis spectrum, corresponding to a bandgap energy of approximately 2.6-3.0 eV. The exact location of the optical absorption edge and the bandgap energy of g-C_3N_4 may fluctuate based on parameters such as the synthesis technique, polymerization degree, sample preparation, and measurement conditions[41]. The production process, doping degree, and concentration of Fe_3O_4 nanoparticles influence the OAE and bandgap energy of the Ag/g-C_3N_4/Fe_3O_4 nanocomposite. The Ag/g-C_3N_4/Fe_3O_4 nanocomposites demonstrate a red shift in the optical absorption edge relative to pure g-C_3N_4, leading to augmented visible light absorption and improved photocatalytic activity. This investigation revealed that the bandgap energy of pure g-C_3N_4 is between 2.6 and 3 eV, while that of the Ag/g-C_3N_4/Fe_3O_4 nanocomposite is 2.36 eV. The OAE for pure g-C_3N_4 is 455 nm, while for the Ag/g-C_3N_4/Fe_3O_4 nanocomposite, it is 650 nm. The alterations in the optical characteristics of the Ag/g-C_3N_4/Fe_3O_4 nanocomposite, in contrast to pure g-C_3N_4, enhance the catalyst's activity in the visible spectrum and improve process efficiency. Prior studies showed similar results about the changes in the optical properties of carbon nitride during the creation of the composite[39]. The observed red shift in the absorption edge of Ag/g-C_3N_4/Fe_3O_4 is attributed to the synergistic effects of Ag and Fe_3O_4. The introduction of Ag nanoparticles induces localized surface plasmon resonance (LSPR), which enhances light absorption in the visible region. Additionally, Fe_3O_4, with its narrower bandgap, serves as a co-catalyst, further extending light absorption and promoting effective charge separation. Furthermore, the reduction in bandgap energy facilitates easier excitation of electrons, reducing the recombination of charge carriers and enhancing photocatalytic activity. The decrease in bandgap leads to enhanced production of reactive oxygen species under visible light, which is a crucial factor in antibiotic degradation. This improved photo-response confirms that Ag/g-C_3N_4/Fe_3O_4 is an efficient visible-light-driven photocatalyst, offering superior performance compared to pure g-C_3N_4.

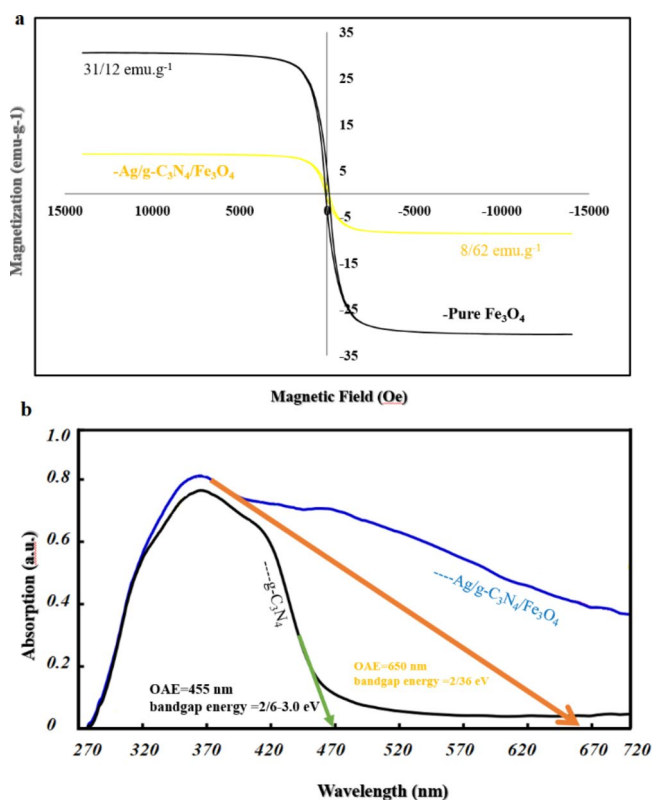**Fig. 6**. (**a**) VSM of Fe_3O_4 and Ag/g-C_3N_4/Fe_3O_4 nanocomposite. (**b**) UV-vis diffuse reflectance spectra of pure g-C_3N_4 and Ag/g-C_3N_4/Fe_3O_4 nanocomposite (Drawn with: Origin Pro, Ver: 10.1.0.178).
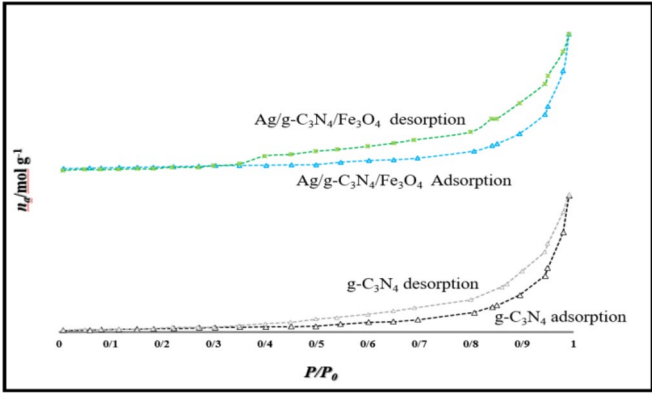
Fig. 7. Adsorption/ desorption isotherm of pure g-C_3N_4 and Ag/g-C_3N_4/Fe_3O_4 nanocomposite. (Drawn with: Origin Pro, Ver: 10.1.0.178).

Components	Surface area (m²/g)	Mean pore diameter (nm)	Total pore volume (cm³/g)
Pure g-C_3N_4	10.8	14.5	0.27
Fe_3O_4	15.2	13.1	0.36
g-C_3N_4/Fe_3O_4	45.3	16.3	0.2

Table 2. Textural properties of pure g-C_3N_4, Fe_3O_4, and Ag/g-C_3N_4/Fe_3O_4 nanocomposite.

The specific surface area of the pure g-C_3N_4 and Ag/g-C_3N_4/Fe_3O_4 nanocomposite was determined using N_2 adsorption-desorption tests and BET analysis, as shown in (Fig. 7). The pristine g-C_3N_4 and Ag/g-C_3N_4/Fe_3O_4 nanocomposite demonstrate a type IV N_2 adsorption-desorption isotherm featuring an H_3 hysteresis loop.

Table 2 outlines the parameters related to the pore structure of pure g-C_3N_4, Fe_3O_4, and the Ag/g-C_3N_4/Fe_3O_4 nanocomposite. The findings demonstrated that the alterations in surface area are substantial, with the Ag/g-C_3N_4/Fe_3O_4 nanocomposite exhibiting a greater surface area (45.3 m²/g) compared to pure g-C_3N_4 (10.8 m²/g) and Fe_3O_4 (15.2 m2/g). Nonetheless, there was merely a minor modification in the average pore diameter and overall pore volume. In Xu and coworkers study, similar results reported[42]. The photocatalytic performance of a material is strongly influenced by its surface area and pore structure. A higher surface area facilitates enhanced light absorption, increases the number of active sites, and promotes better interaction between the photocatalyst and pollutant molecules. The significant increase in surface area observed in the Ag/g-C_3N_4/Fe_3O_4 nanocomposite compared to pure g-C_3N_4 suggests improved adsorption capacity, which enhances the degradation efficiency of antibiotics. Moreover, the mesoporous structure (as confirmed by the H3 hysteresis loop) plays a crucial role in the mass transfer of reactants and intermediates. The optimal pore size distribution ensures efficient diffusion of molecules, thereby reducing diffusion limitations and allowing better utilization of photoinduced charge carriers. The presence of Fe_3O_4 also contributes to enhanced charge separation and charge transfer efficiency, which, coupled with the increased surface area, further improves photocatalytic activity. Thus, the BET results validate the improved photocatalytic efficiency of the Ag/g-C_3N_4/Fe_3O_4 nanocomposite by demonstrating a larger surface area, better pollutant adsorption, and effective charge carrier utilization[43].

Process optimization
The statistical analysis and interaction of parameters
A statistical examination of the observed responses was conducted to determine the conditions that enhance the degradation of ceftriaxone and azithromycin by PCP. The primary parameters and designated ranges are outlined in Table 1. The findings indicate that PCP demonstrates substantial efficacy in the degradation of ceftriaxone, ranging from 29.4 to 92.8%, with an average of 57.79% and azithromycin degraded ranging from 19.8 to 81%, with an average of 47.56%. The runs of PCP presented in table. S1.

The fitting findings from Design Expert software (Ver: 10.1.03.2, www.statease.com/software/design-expert) indicate that the quadratic model is offered for the optimization of PCP in antibiotics degradation (Tab. S2). Fisher variance ratios and P-values are established statistical metrics employed in ANOVA analysis to adjust factor fitting for deviations. The ANOVA results demonstrate a robust quadratic regression model with a valid coded relationship between actual and predicted values, as evidenced by a high reliability and low probability value in Table 3.

Table 3 reveals that the ANOVA findings for the quadratic regression model demonstrate excellent reliability and a low probability value, indicating that the correlation between actual data and predicted values is justifiable. The correlation coefficient values (i.e., R2, R^2_{adj}, and $R^2_{predict}$) significantly exceeded those of alternative models, thereby affirming the model's exceptional validity and efficacy. A perfect correlation exists among R^2, R^2_{adj}, and $R^2_{predict}$, signifying the model's proficiency in properly predicting answers[44,45].

Source	Sum of squares	df	Mean square	F-value	p-value	
Azithromycin						
Model	7623/46	14	544/53	394/91	< 0.0001	Significant
Residual	19/30	14	1/38			
Lack of Fit	16/81	10	1/68	2/70	0/1756	Not significant
Pure Error	2/49	4	0/6230			
Cor Total	7642/77	28				
Ceftriaxone						
Model	7580/88	14	541/49	204/68	< 0.0001	Significant
Residual	37/04	14	2/65			
Lack of Fit	29/95	10	2/99	1/69	0/3235	Not significant
Pure Error	7/09	4	1/77			
Cor Total	7617/92	28				

Table 3. ANOVA for the quadratic model of PCP in antibiotics removal.
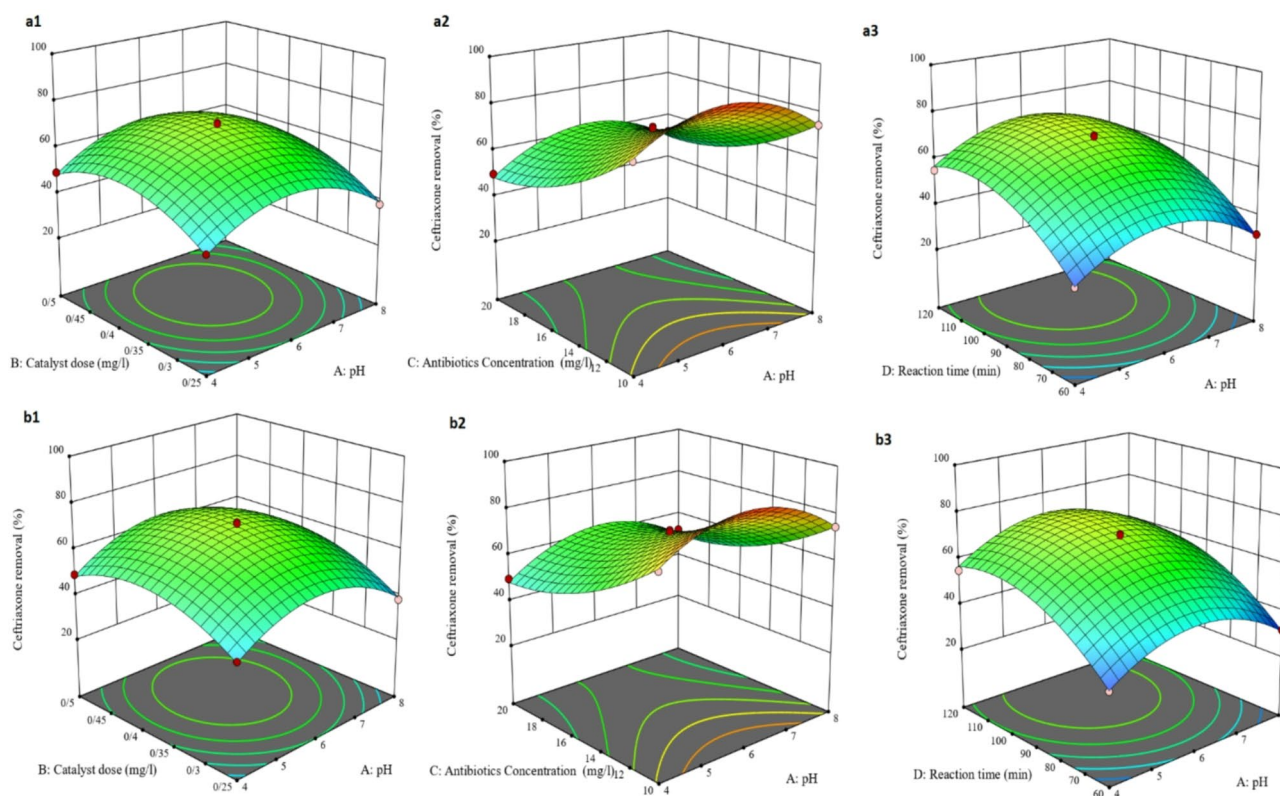

Fig. 8. , exhibited the effect of parameters on the PCP performance. The influence of each parameter on the effectiveness of removal is significant.

As explained below, the polynomial equation related to antibiotics removal (%) is represented as coded factors (Eqs. (11), (12)).

$$Azithromycin\ deg\,radation\,(\%): 59/96 + 0/04 \times A + 4/49 \times B - 13/4 \times C + 12/48 \times D - 2/175 \times BC \\ - 0/125 \times BD - 14/3 \times A^2 - 10/8 \times B^2 + 7/36 \times C^2 - 12/1 \times D^2 \tag{11}$$

$$Ceftriaxone\ deg\,radation\,(\%): 70/32 - 0/24 \times A + 4/39 \times B - 13/5 \times C + 12/55 \times D - 0/6 \times BD \\ - 14/5 \times A^2 - 11/1 \times B^2 + 6/9 \times C^2 - 11/5 \times D^2 \tag{12}$$

The effect of factors on the antibiotics removal
Figure 8 Effect of parameters (pH, dose, ceftriaxone and azithromycin concentration and reaction time) into antibiotics degradation in PCP- Ag/g-C_3N_4/Fe_3O_4 system. (Drawn with: Design Expert software, Ver: 10.1.03.2).

pH effect   The solution's pH can significantly influence the photocatalytic performance (PCP) in the degradation of both antibiotics. According to Fig. 8a1 and b1, the performance of the PCP improved with an increase in the solution's pH from acidic conditions to near-neutral pH. However, as the reaction medium became more alkaline, the effectiveness of the PCP diminished significantly.

The solution's pH can influence the photocatalytic process in several ways. Initially, it may alter the surface charge of the catalyst, which in turn affects the adsorption of reactants on its surface, thereby impacting the reaction rate. Additionally, pH can regulate the rate of electron-hole recombination, reducing the efficacy of the photocatalytic process. Moreover, the pH level influences the stability of the catalyst, affecting its performance over time. As a result, pH significantly impacts the absorption capacity and decomposition of organic compounds, as well as the electrical distribution on the catalyst surface and the valence band oxidation potential[46,47].

Two key factors influencing the efficiency of PCP, related to the solution's pH, are the catalyst's zero-point charge (pH_{zpc}) and the pollutant's acid dissociation constant (pKa)[48]. The pH_{zpc} denotes the pH at which the catalyst's surface exhibits a neutral charge, possessing an equal distribution of positive and negative charges. Understanding the zero-point charge is crucial for comprehending the surface chemistry of photocatalysts. The influence of pH_{zpc} on PCP performance suggests that the surface charge of the photocatalyst directly affects the adsorption of reactants. A positively charged photocatalyst can attract negatively charged species, such as anions, whereas a negatively charged photocatalyst attracts positively charged species, such as cations. At the zero-point charge, adsorption is typically less favorable[49].

Furthermore, the zero-point charge can influence photocatalyst stability. A positively or negatively charged surface induces electrostatic repulsion among catalyst particles, preventing aggregation and enhancing performance. Conversely, at a neutral charge, particles may exhibit a higher tendency to aggregate, reducing photocatalytic efficiency. Moreover, the zero-point charge affects the electron-hole recombination rate. When the photocatalyst has a net positive or negative charge, charge separation is facilitated, reducing electron-hole recombination and improving efficiency. However, when the surface charge is neutral, recombination rates increase, leading to diminished photocatalytic activity[50].

The pH_{zpc} of the Ag/g-C_3N_4/Fe_3O_4 nanocomposite is 6.89, indicating that at pH levels below this threshold, the catalyst surface is predominantly occupied by H + ions, whereas at pH levels above this value, OH − ions dominate. Consequently, the highest efficiency of the process is expected under slightly acidic conditions compared to other pH values.

The pKa of organic contaminants significantly influences PCP performance by determining the extent of ionization in solution. Organic pollutants with lower pKa values exhibit stronger acidity and exist predominantly in their protonated form under acidic conditions, while those with higher pKa values exist primarily in their deprotonated form under basic conditions[51]. The pKa value affects pollutant adsorption onto the photocatalyst surface and subsequent photocatalytic degradation. For instance, in acidic solutions, antibiotics with low pKa values exhibit increased affinity for positively charged photocatalyst surfaces due to electrostatic interactions, which can enhance adsorption and degradation. However, very low pH may also hinder photocatalytic efficiency by altering charge interactions and affecting the stability of reactive species[52].

The pKa values of azithromycin are 8.1 and 8.8, while ceftriaxone exhibits pKa values of 3.0, 3.2, and 4.1, respectively. The low pKa values of antibiotics indicate strong acidity, leading to their predominant protonated form in acidic conditions. This can impact their adsorption behavior on the photocatalyst surface and subsequent degradation. Results indicate a strong correlation between pH levels and PCP efficiency in antibiotic degradation. Increasing the pH from 4.0 to neutral enhances PCP efficiency, whereas under alkaline conditions, efficiency declines. A solution pH of 5.2 is recommended as the optimal condition for photocatalysis.

In a study by Fadillah et al., the photocatalytic performance improved under acidic conditions. Similarly, Mehrabadi et al. examined the effect of pH on the degradation of 2,4-D over a pH range of 3.0 to 10.0, determining that the highest degradation efficiency occurred at pH 6 [53].

Catalyst dose effect   Another component that significantly influences the PCP is the catalyst dosage. The impact of these parameters is depicted in (Fig. 8a1 and b1). The findings indicate that increasing the catalyst dosage from 0.25 to 0.5 g/L leads to a significant improvement in process efficacy, followed by a subsequent decline. Increasing the catalyst dosage enhances the number of accessible active sites on the catalyst surface, hence potentially improving the effectiveness of the PCP. The augmented surface area of the catalyst can result in a greater concentration of reactive species, such as hydroxyl radicals, so improving the breakdown of antibiotics. A greater catalyst dosage can diminish the recombination rate of electron-hole pairs, hence enhancing photocatalytic efficiency. Nonetheless, elevating the catalyst dosage beyond a specific threshold may adversely impact PCP efficiency. At very high catalyst dosages, the catalyst particles may combine and form bigger particles, which can diminish the available surface area for photocatalytic processes. This may result in diminished efficiency and potentially obstruct the photocatalytic process. Furthermore, a high catalyst dosage may result in a turbid solution due to dispersed catalyst particles, potentially diminishing the efficacy of the PCP[54]. Determining the appropriate catalyst dosage for a certain photocatalytic reaction relies on various aspects, including the characteristics of the catalyst material, the attributes of the pollutant being degraded, and the experimental settings. The findings suggest an optimal catalyst dosage of 0.42 g/L. Prior research has indicated varying catalyst dosages in the PCP for optimal pollutant removal. All investigations share a common characteristic: the impact of varying catalyst dosages on process efficiency. In the majority of research, the pattern of impact initially rises and then subsequently declines[55,56].

Concentration of antibiotics effect   Azithromycin and ceftriaxone are utilized in varying concentrations to manage human infections. Consequently, varying concentrations of both antibiotics may be present in the environment. The concentration of these antibiotics can significantly impact the PCP. Different degrees of intake

pollution lead to differing reaction speeds; thus, the starting concentrations are a critical factor influencing the efficiency of the PCP. In current investigation, the concentration of 10–20 mg/L of antibiotics was chosen and the performance of the PCP was studied. The data reveal a negative association between the concentration of pollutants and the efficacy of the procedure (Fig. 8a2 and b2). The rate of adsorption of pollutants onto the photocatalyst's surface is affected by the initial concentration of pollutants. A diminished initial concentration leads to slower adsorption, whereas an elevated starting concentration accelerates adsorption. High pollutant concentrations can saturate photocatalyst active sites, reducing adsorption and efficiency. This occurrence is referred to as catalyst toxicity or deactivation. The adsorption of antibiotic molecules onto the catalyst surface is exactly proportional to the initial concentration of the antibiotics. Nonetheless, the generation of $OH^{\bullet}$ and $O_2^{\bullet-}$ radicals on the catalyst surface remained stable. As a result, the relative concentration of $OH^{\bullet}$ and $O_2^{\bullet-}$ radicals targeting the azithromycin and ceftriaxone molecules diminished[57]. Moreover, elevated initial concentrations of pollutants may result in the generation of intermediates that can obstruct the photocatalytic process. The ideal initial concentration of pollutants in PCP is contingent upon various aspects, including the characteristics of the photocatalyst, the intensity of the light source, and the individual experimental settings[58]. In current study, 10 mg/L of antibiotics proposed at suitable concentration to PCP performance.

<u>Reaction time effect</u> The reaction time, or the duration of the photocatalytic process, can significantly influence the efficiency of photocatalytic degradation. The reaction time of the PCP dictates the duration available for the photocatalyst to produce reactive species and facilitate the breakdown of pollutant molecules. The current study examined the impact of these characteristics for a duration of 60 to 120 min. The Findings (Fig. 8a3 and b3) shows with increasing the reaction time, more antibiotics degrading and the performance of PCP is high. Initially, the degradation rate of pollutants in the PCP is generally modest, as the photocatalyst requires time to produce adequate reactive species to initiate the degradation process. As reaction time increases, the availability of reactive species rises, resulting in an elevated rate of pollutant breakdown. The enhancement in pollutant degradation rates may persist up to a specific threshold, beyond which efficiency gains could plateau due to factors including catalyst deactivation or the saturation of active sites on the catalyst surface[59]. Nonetheless, extending the reaction period beyond a specific threshold may not result in additional enhancements in the efficiency of the photocatalytic process. If the initial concentration of the pollutant is little, the reaction may be constrained by photon availability, and extending the reaction time may not result in substantial enhancements in photocatalytic efficiency. The properties of the photocatalyst, the intensity of the light source, the initial concentration of the pollutant, and the specific experimental settings are common factors that influence reaction time[60]. The optimal reaction time for antibiotics the decomposition is 107 min.

Ultimately, after optimizing PCP using the BBD method, the best conditions were established at a pH of approximately 5.2, with a catalyst dosage of 0.42 g/L, a reaction duration of 107 min, and a starting antibiotic concentration of 10 mg/L. Under these optimized conditions, PCP demonstrated the ability to achieve 83.3% ± 2.1% and 93.3% ± 1.8% degradation of azithromycin and ceftriaxone, respectively. These results were obtained from triplicate experiments, ensuring statistical reliability and reproducibility.

Other studies in optimal conditions

Synergistic effect

The function of all employed mechanisms in PCP for antibiotic degradation in the two systems was examined both separately and concurrently under ideal conditions. Adsorption and photolysis (UV-C, UV-A, and visible light) were influential mechanisms in PCP. All pathways exhibited significantly low efficiency in the breakdown of antibiotics individually. For the ceftriaxone antibiotic, the efficiencies of sorption, UV-A, UV-C, visible light photolysis, PCP (UV-C), PCP (UV-A), and PCP (visible light) were 12%, 15%, 27%, 10%, 98%, 93%, and 72%, respectively. The SF coefficients for PCP(UV-A), PCP(UV-C), and PCP(Vis) were examined as 4.36, 2.57, and 4.23, respectively. And for the azithromycin antibiotic, the efficiencies of sorption, UV-A, UV-C, visible light photolysis, PCP (UV-C), PCP (UV-A), and PCP (visible light) were 9%, 13%, 24%, 8%, 95%, 83%, and 69%, respectively. The SF coefficients for PCP(UV-A), PCP(UV-C), and PCP(Vis) were examined as 4.2, 2.17, and 3.9, respectively. The combination of light and the catalyst enhanced antibiotic degradation via indirect oxidation involving free radicals and electron-hole pairs. The augmented effectiveness of the method in the presence of UV-C resulted from improved oxidation by photolysis. In the study by Yu and colleagues, a removal efficiency of 4.64 for Oxytetracycline (OTC) was obtained in the photocatalytic process including SF. The accumulation of electrons on the catalyst and the generation of reactive oxidant species (ROS) were the factors contributing to the synergistic breakdown of OTC through this mechanism[61].

COD and TOC measurements

COD and TOC are acronyms representing distinct metrics for assessing water and wastewater quality. Both techniques are frequently employed to assess the level of organic contamination in water samples. Under ideal conditions, the PCP successfully reduced COD by 65.5% and TOC by 52%. However, due to the possibility of breakdown of antibiotics into intermediates, the reduction of COD and TOC was slower than the degradation of these antibiotics. Enhancing the reaction time was essential for the more effective elimination of COD and TOC. After 240 min, a notable reduction in antibiotics, COD, and TOC was attained (Fig. 9a). These tests can reveal the concentration of organic matter, degree of organic contamination, and treatment efficiency. The study by Aanchal Rather and colleagues revealed a reduction of 72% in metronidazole levels, 68% in COD, and 62% in TOC[62].
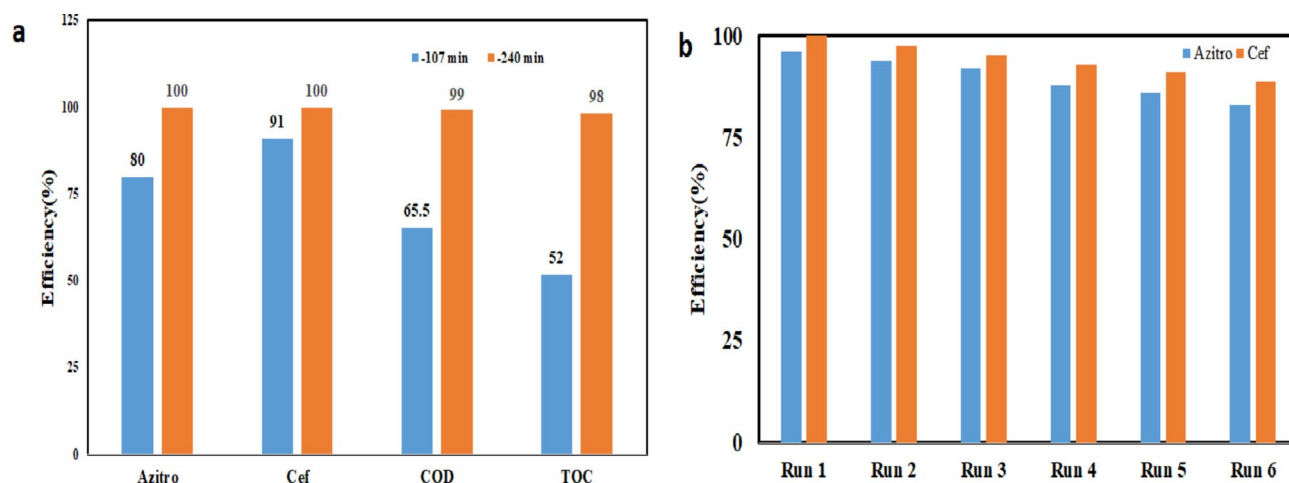
Fig. 9. (**a**) COD and TOC removal efficiency, (**b**) Reusability of catalyst (pH = 5.2, RT = 107 min, antibiotics concentration = 10 mg/L, and catalyst dose = 0.42 g/L) in PCP- Ag/g-C$_3$N$_4$/Fe$_3$O$_4$ system. (Drawn with: Origin Pro, Ver: 10.1.0.178).

Reusability of catalyst

The reusability of catalysts is a critical consideration in the development and optimization of the PCP for environmental remediation and many applications. Through the investigation of catalyst reusability, researchers and engineers can gain insights into the sustained performance and efficiency of PCP, hence formulating solutions for process optimization and enhancement. The ability to utilize the PCP in a real-scale and environmental setting is heavily reliant on the stability of the catalyst and the overall performance of the process. The results shown in (Fig. 9b) indicate that the efficacy of the PCP in eliminating antibiotics remained mostly unchanged even after the sixth cycle of visible light irradiation. The process efficiency declined by 13% and 12.7% for azithromycin and ceftriaxone, respectively, throughout six successive phases. The expense of manufacturing photocatalysts can be substantial. The reutilization of a catalyst can diminishes expenses and enhance economic feasibility. The ecological consequences of photocatalyst manufacturing and disposal can be mitigated through the reutilization of catalysts. Moreover, it is significant that the effectiveness of photocatalysts may decline over time due to catalyst deactivation or fouling. Moreover, the reapplication of a catalyst may function as an essential instrument in assessing its enduring performance and efficacy. Ultimately, photocatalytic techniques for environmental remediation frequently necessitate substantial amounts of catalyst material, and employing a catalyst that can be reutilized numerous times can aid in the scalability of the process[63]. Balakrishnan and colleagues revealed that PCP employing g-C$_3$N$_4$ has shown exceptional stability, and the catalysts have displayed reusability throughout multiple cycles[64].

Light intensity

Light intensity is a crucial factor in the PCP as it plays a key role in providing the necessary energy for generating reactive species by the photocatalyst and subsequently degrading pollutants. As examined in this study, light intensities of 15, 30, and 60 mW/cm^2 were tested, and the results indicated that increasing light intensity enhances the efficiency of the photocatalytic process in the removal of ceftriaxone and azithromycin. Increasing light intensity leads to a higher generation rate of electron-hole pairs on the photocatalyst surface, resulting in the increased production of ROS such as hydroxyl radicals, superoxide, and hydrogen peroxide, which effectively degrade pollutant molecules. According to the obtained results, light intensities of 15, 30, and 60 mW/cm^2 resulted in the removal of 69%, 80%, and 97% of ceftriaxone, and 78%, 91%, and nearly 100% of azithromycin, respectively. However, the photocatalytic process does not always respond linearly to increasing light intensity, and there is an optimal value beyond which the efficiency may stabilize or decrease. At intensities exceeding this optimal level, photocatalyst surface saturation, increased electron-hole recombination, and thermal effects may reduce the process efficiency. Other limiting factors include particle shadowing in the reaction medium, reduced light penetration into deeper photocatalyst layers, and thermal influences that can negatively impact the process. Photocatalyst characteristics, Wavelength and intensity of the light source, Concentration and properties of the pollutant, Angle and orientation of the light source, Distance between the light source and the photocatalyst, and Presence of light-absorbing or scattering materials are factors that influence on the optimal light intensity[65]. Moradi and coworkers evaluated the influence of light intensity (15–60 mW/cm^2) on the deactivation of Escherichia coli in PCP. The data imply that boosting the light intensity leads to a decrease in the demand time[66].

Kinetics study

A model based on empirical evidence was constructed to describe the chemical degradation of antibiotics in PCP system. The model, represented by (Eq. 6), was developed under optimized conditions while considering different antibiotic concentrations. A graphical representation of antibiotics degradation over PCP is presented in (Fig. S1) and (Tab. S3), illustrating the kinetic behavior of the process. The degradation kinetics followed a

pseudo-first-order model, as determined by fitting the experimental data to a linear first-order kinetic equation. In a first-order kinetic model, the rate of reaction is directly proportional to the concentration of the reactant, meaning that higher reactant concentrations lead to an increased reaction rate. This behavior is commonly observed in photocatalytic degradation processes, where the active sites on the photocatalyst surface play a crucial role in reaction progression[67]. In the PCP system, this kinetic behavior is attributed to the availability of reactive species such as hydroxyl radicals and superoxide anions, which facilitate the degradation of antibiotic molecules. The presence of competitive adsorption effects, recombination rates of charge carriers, and variations in catalyst surface properties may also influence the observed kinetics. Similar kinetic behavior has been reported in previous studies. For instance, Balakrishnan et al. demonstrated that the photocatalytic degradation of 2,4-D herbicide followed pseudo-first-order kinetics. This suggests that, under photocatalytic conditions, many organic contaminants, including antibiotics, exhibit a reaction rate that is primarily governed by their surface interactions with the photocatalyst and the generation of reactive oxidative species[68].

Radical scavengers effect
Radical scavengers play a crucial role in PCP by modulating the availability of reactive oxygen species (ROS). These molecules interact with ROS, such as hydroxyl radicals, superoxide anions, and photogenerated holes, thereby neutralizing them before they can participate in pollutant degradation. The presence of radical scavengers can significantly influence the overall photocatalytic performance, either by selectively quenching certain ROS or by altering charge carrier dynamics. In this study, the impact of radical scavengers on PCP efficacy in antibiotics degradation was evaluated using methanol (CH_3OH), tert-butanol (t-BuOH), and potassium iodide (KI). The results, summarized in Table 4, demonstrate the varying degrees of inhibition exerted by these scavengers. Among them, tert-butanol exhibited the most pronounced inhibitory effect, suggesting that hydroxyl radicals play a dominant role in the degradation process. Conversely, methanol had the least impact, indicating its lower specificity for scavenging surface-bound hydroxyl radicals compared to freely diffusing ones. To elucidate the role of each scavenger, the following chemical reactions (Eqs. 13–17) describe their interactions with ROS and charge carriers within the PCP system[69].

$$I^- + h_{vb}^+ \rightarrow heat \tag{13}$$

$$2I^- + e_{cb}^- \rightarrow I_2 \tag{14}$$

$$I^- + OH_{ads}^{\cdot} \rightarrow I^{\cdot} + OH_{ads}^- \tag{15}$$

KI acts as an effective (h^+) scavenger, removing photogenerated holes before they contribute to ROS formation. This results in a reduction of oxidative species, leading to diminished antibiotics degradation efficiency. The reduction in PCP efficiency in the presence of KI confirms that photogenerated holes contribute significantly to ROS formation.

$$t-BuOH + OH^{\cdot} \rightarrow t-BuO\cdot + H_2O \tag{16}$$

		Reaction time (min)						
	Radicals scavengers	0	10	20	40	60	80	100
Azitro	Tert-butanol	0	5.6	11.1	20	31.8	43.2	45
Cef		0	8.9	14.9	28.4	39.8	48	53
Azitro	KI	0	11.5	20.2	32.8	44.4	52	57
Cef		0	17.6	29	38	52	64.2	63
Azitro	methanol	0	15.5	25.6	39	55	68.8	69
Cef		0	19.8	30	43.3	65	73.1	72
Azitro	No scavengers	0	24.3	42.6	60.5	72.3	85.5	80
Cef		0	32.2	55.8	65.6	75.6	91.2	91
	Anions	0	10	20	40	60	80	100
Azitro	PO4	0	6.8	12.3	22	34.5	44.5	49
Cef		0	12	19	31.8	41.3	50.2	55
Azitro	CO3	0	14.5	24.8	35.6	48.9	58	59.9
Cef		0	19.8	32.3	41.8	55	66.4	67
Azitro	SO4	0	18.7	28.8	42	58	72	72
Cef		0	22.5	32.3	45	68.7	76.7	76
Azitro	No Anions	0	24.3	42.6	60.5	72.3	85.5	80
Cef		0	32.2	55.8	65.6	75.6	91.2	91

Table 4. Quenching test, and d) anions effect (pH = 5.2, rt = 107 min, antibiotics concentration = 10 mg/l, and catalyst dose = 0.42 g/L).

16

Tert-butanol is a well-known scavenger of hydroxyl radicals, particularly those generated in the bulk solution. Its strong inhibitory effect in this study suggests that hydroxyl radicals are the primary oxidizing agents in the antibiotic degradation process. The significant decrease in degradation efficiency upon t-BuOH addition confirms that the reaction pathway is predominantly hydroxyl radical-mediated.

$$CH_3OH + OH^{\cdot} \rightarrow CH_3O + OH^- \tag{17}$$

Methanol can also scavenge hydroxyl radicals, but its lower impact on PCP efficiency suggests that it primarily reacts with free hydroxyl radicals in solution rather than surface-bound radicals. Since surface-bound hydroxyl radicals are generally more reactive, the minimal effect of methanol implies that surface-driven oxidation plays a key role in PCP efficiency.

The results of this study reinforce the critical role of hydroxyl radicals in the PCP-mediated degradation of antibiotics. The strong inhibitory effect of tert-butanol confirms that hydroxyl radicals are the dominant ROS, while the moderate effect of KI suggests that photogenerated holes also contribute to the reaction pathway. Methanol's limited influence highlights the importance of surface interactions, as freely diffusing hydroxyl radicals play a less significant role compared to surface-bound species. Furthermore, these findings provide insights into optimizing photocatalytic conditions for wastewater treatment applications. By understanding the dominant ROS and their interactions with scavengers, strategies can be developed to enhance photocatalyst performance, such as modifying the surface properties to promote the generation of specific ROS or employing co-catalysts to suppress charge recombination. Prior research assessing the effects of radical scavengers has recognized the experiments conducted by Yang and colleagues, as well as those by Shyamala and associates. The OH$^{\bullet}$ has been recognized as the primary active radical in the PCP[70,71].

Inorganic anions effect

Inorganic anions are prevalent in aquatic environments and can significantly impact photocatalytic performance. Their effects depend on several factors, including the type and concentration of anions, the characteristics of the photocatalyst material, and the specific pollutant being degraded. This study examined the effects of PO_4^{3-}, CO_3^{2-}, and SO_4^{2-}. The investigation's results (Table 4) reveal the significant inhibitory impact of PO_4^{3-}, leading to efficiency reductions of 55% and 49% for azithromycin and ceftriaxone, respectively. In contrast, the presence of the SO_4^{2-} has the least impact on the efficacy of the PCP performance.

One key factor affecting anion interference is the modification of surface charge distribution on the photocatalyst. At alkaline pH levels, negatively charged anions (e.g., PO_4^{3-}, CO_3^{2-}) tend to adsorb onto the photocatalyst, reducing the positive surface charge and thereby decreasing electrostatic attraction for negatively charged pollutants. This decrease in zeta potential results in lower pollutant adsorption and reduced photocatalytic efficiency. Some anions can react with ROS, particularly hydroxyl radicals ($^{\bullet}OH$), reducing their concentration and limiting the degradation of organic pollutants. Carbonate radicals ($CO_3^{\bullet-}$) have a significantly lower oxidation potential than hydroxyl radicals, making them less effective in degrading pollutants.

Energy efficiency

The EE/O is a metric employed to assess the energy efficiency of a PCP. It is defined as the electrical energy necessary to eliminate one order of magnitude of the target pollutant from a certain volume of solution. The EE/O can be utilized to assess energy efficiency in order to enhance the operational parameters of a certain process. A reduced EE/O number signifies a more energy-efficient process. The EE/O for the PCP was computed at the optimal rate of 17.3 KW/h.m^3, as per Eq. 8. In the study by Elbadawy and colleagues, the energy efficiency/optimum (EE/O) of photocatalytic degradation of textile dye was reported as 20 kWh/m^3/order[72].

Hospital wastewater test

This section of the study assessed the efficacy of the optimized photocatalytic process in an actual environment (hospital wastewater). The physicochemical characteristics of hospital wastewater are presented in Table S4.The photocatalytic process was examined on the effluent following biological sedimentation (prior to chlorination) and the effluent from the chlorination unit. The results are illustrated in (Fig. 10). The results indicate a significant reduction in the efficiency of the photocatalytic process for the removal of antibiotics from hospital wastewater. Various explanations such a presence of complex organic compounds and matrix (pharmaceuticals, metabolic products, detergents, and natural organic matter), inorganic constituents' inhibitory effects, turbidity and reduced UV light penetration, dyes and chromophores interference, stable By-products formation, antioxidant compounds inhibitory, reaction competition and incomplete removal of macro and micro pollutants can be posited for these outcomes[73]. The results showed that the presence of significant amounts of chlorine or chlorinated compounds in wastewater reduces the efficiency of photocatalytic processes. This is due to the production of reactive chlorine species (RCS) such as hypochlorite, chlorine gas, and chlorate, which are less reactive than hydroxyl radicals. Chlorine and its compounds also act as scavengers for hydroxyl radicals, limiting their availability for pollutant degradation. Additionally, persistent and toxic chlorinated byproducts, like chloroform and trichloroacetic acid, form during the process, which are harder to degrade. Moreover, chlorine compounds absorb UV light and block photocatalyst active sites, further reducing the overall efficiency[74].

Photocatalytic degradation mechanism of antibiotics

A hypothesis for the degradation of antibiotics by PCP has been proposed, and a diagrammatic representation is illustrated in (Fig. 11). The synthesized nanocomposite containing Ag, g-C_3N_4, and Fe_3O_4 has unique characteristics and particular activities. The catalytic efficacy of Fe_3O_4 inside an Ag/g-C_3N_4/Fe_3O_4 nanocomposite is contingent upon various parameters, including the synthesis technique, the characteristics of the precursor
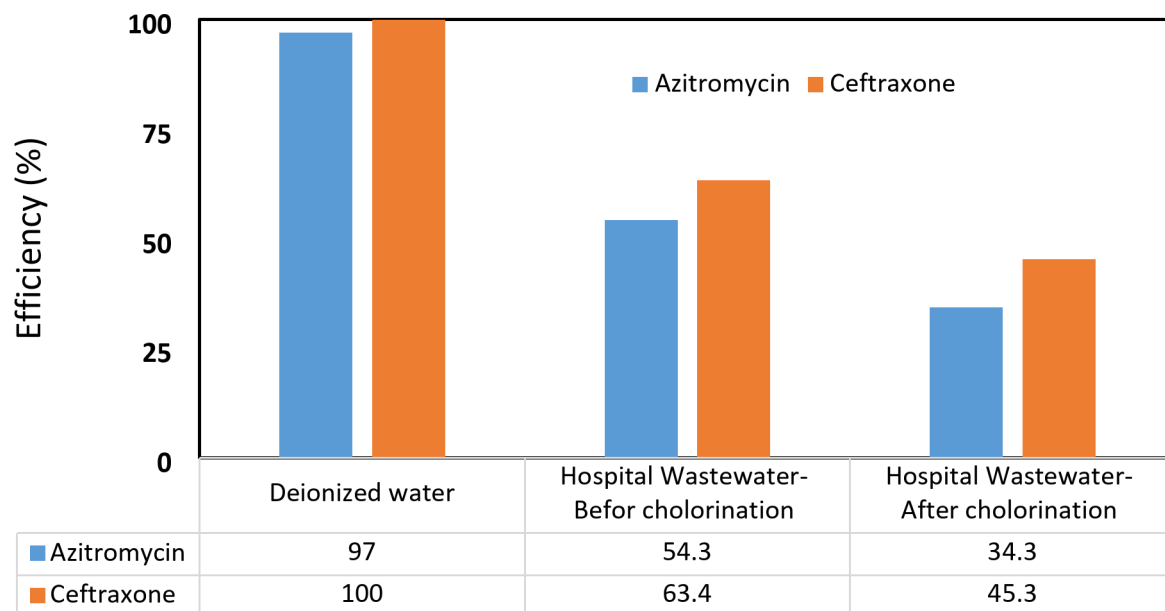
Fig. 10. Efficiency of the photocatalyst in the hospital wastewater (pH = 5.2, RT = 107 min, antibiotics concentration = 10 mg/L, and catalyst dose = 0.42 g/L) in PCP- Ag/g-C$_3$N$_4$/Fe$_3$O$_4$ system. (Drawn with: Origin Pro, Ver: 10.1.0.178).
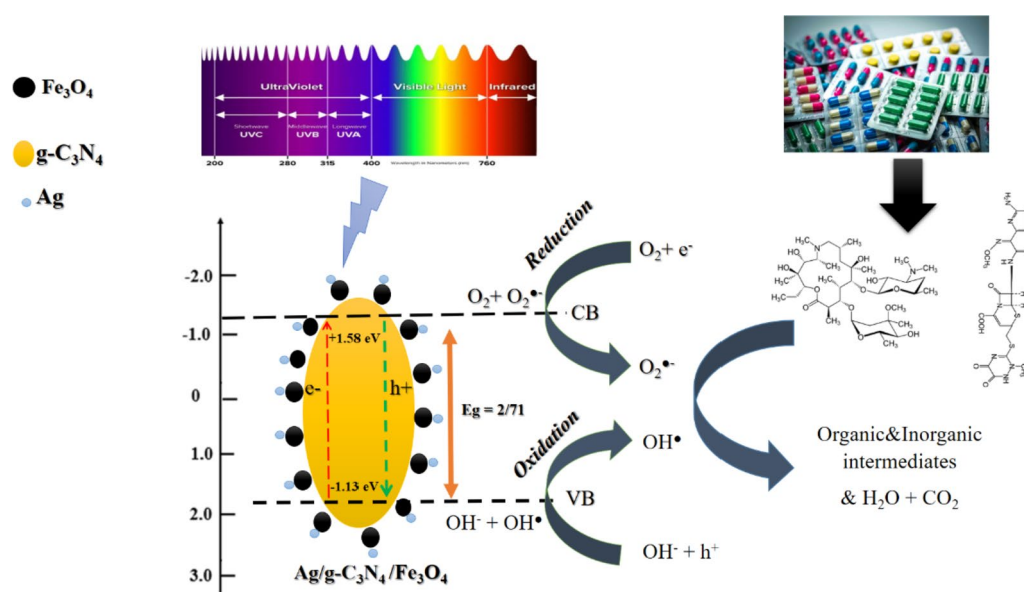
	Deionized water	Hospital Wastewater-Befor cholorination	Hospital Wastewater-After cholorination
Azitromycin	97	54.3	34.3
Ceftraxone	100	63.4	45.3

Fig. 11. Mechanism of antibiotics degradation by the PCP- Ag/g-C$_3$N$_4$ /Fe$_3$O$_4$. (Drawn with: EdrawMax Ultimate, Ver: 14.2.2.1269).

materials, and the particular reaction circumstances. Fe$_3$O$_4$ is frequently employed as a co-catalyst in g-C$_3$N$_4$-based photocatalysts owing to its capacity to enhance charge separation and improve the transfer of photo-generated electrons and holes. Fe$_3$O$_4$ functions as an electron sink, diminishing the recombination rate of charge carriers and enhancing the overall efficiency of the PCP. The particular activity of Fe$_3$O$_4$ in the Ag/g-C$_3$N$_4$/Fe$_3$O$_4$ nanocomposite can be assessed by its capacity to generate reactive oxygen species and breakdown contaminants under light. The specific activity of Fe$_3$O$_4$ can be influenced by variables like loading amount, particle size, and distribution of Fe$_3$O$_4$ within the g-C$_3$N$_4$ matrix[75,76]. g-C$_3$N$_4$ is an extensively researched photocatalytic material recognized for its capacity to generate reactive oxygen species and decompose contaminants when exposed to light. In the g-C$_3$N$_4$/Fe$_3$O$_4$ nanocomposite, the g-C$_3$N$_4$ component serves as the principal photocatalyst ingredient. The specific activity of g-C$_3$N$_4$ is influenced by parameters like crystallinity, surface area, and bandgap energy of the material[77]. Ag fulfills multiple critical functions in photocatalysts, including plasmonic

effects, charge separation, acting as an active site for redox reactions, and exhibiting synergistic effects with other materials (e.g., g-C_3N_4 or TiO_2)[39].

The light irradiation facilitates the passage of photoinduced electrons from the conduction band of g-C_3N_4 to those of Fe_3O_4 and Ag. The CB level of Fe_3O_4 is positioned below that of g-C_3N_4, leading to an energy-aligned band structure in the Ag/g-C_3N_4/Fe_3O_4 nanocomposite system. Furthermore, due to the high conductivity of Fe_3O_4, the rate of electron transport is enhanced, therefore hindering the direct recombination of photoinduced electron-hole pairs in the Ag/g-C_3N_4/Fe_3O_4 nanocomposite hybrid structure. Consequently, Ag and Fe_3O_4 serve as acceptors of the photoinduced electrons generated by g-C_3N_4. Thus, the presence of Fe_3O_4 at the interface significantly diminishes the likelihood of photoinduced electron-hole pair recombination, allowing for an increased generation of charge carriers that produce reactive species. The electrons in the conduction band of Fe_3O_4 demonstrate advantageous reducing capabilities, facilitating the effective reduction of oxygen species adsorbed on the composite catalyst surface into several reactive species (including $O_2^{•-}$, $HO_2^•$, and $HO^•$)[78]. In the Ag/g-C_3N_4/Fe_3O_4 nanocomposite system, the conduction band of g-C_3N_4 is approximately positioned at -1.3 eV, while its valence band is at + 1.6 eV. The CB of Fe_3O_4 is located at a lower energy level than that of g-C_3N_4 which facilitates electron transfer. The presence of Ag, due to its plasmonic effects, enhances charge separation and promotes efficient electron and hole transport, ultimately improving the photocatalytic performance[79].

Mineralization of azithromycin and ceftriaxone antibiotics and by-products studies
GC-MS was employed to examine the intermediates, by-products, and potential reaction pathways of azithromycin and ceftriaxone degradation under ideal circumstances, as outlined in the materials and techniques section. According to the results of GC-MS analysis, the azithromycin and ceftriaxone and several by-products related to these antibiotics were detected. In most instances, the hydroxyl radical serves as the primary reactive species responsible for degradation. This process involves the hydroxylation of the aromatic ring through an electrophilic attack by the •OH radical at various positions of azithromycin, resulting in the cleavage of C—O and C—N bonds, as well as the cleavage at the -position of the aromatic moiety, leading to the formation of ring-opening products[80]. The results in azithromycin degradation indicated that the fragmentation peak at m/z 734.8 corresponds to O-demethylation (TP-A) or N-demethylation (TP-B) of the parent compound; further conversion of these compounds produced two additional products with characteristic peaks at m/z 704.8 (TP-C) and m/z 692.4 (TP-D), respectively. The fragmentation pattern of the parent chemical exhibited a prominent distinctive ion at m/z 592.8, resulting from the sequential cleavage of the amino sugar molecules D-desosamine and L-cladinose. The removal of either D-desosamine or L-cladinose is shown by a distinct peak at m/z 592.8, whilst the simultaneous removal of both molecules is represented by a distinct peak at m/z 432.8. The distinctive peak at m/z 720.9 (TP-E) corresponds to the concurrent O-demethylation and N-demethylation of the parent molecule. The breakdown products of amino sugars are also found in our investigation. The peak at m/z 156.2 corresponds to the cleavage of L-cladinose, resulting in the generation of other minor products with distinctive peaks at m/z 121.1 (TP-M) and m/z 85.3 (TP-N), respectively. Consequently, these findings demonstrated that the synthesized ternary composite could effectively decompose the parent molecule azithromycin into smaller entities under visible light irradiation. The dehydrated derivative of D desosamine (TP-K) and the subsequent elimination of the N-methylenemethanamine fragment produced the peak at m/z 114.2 (TP-L). Conversely, the cleavage of C-O bonds and the ring opening in L-cladinose result in the generation of additional minor products, exhibiting distinctive peaks at m/z 121.1 (TP-M) and m/z 85.3 (TP-N), respectively. Thus, our results suggested that the produced ternary composite could successfully degrade the parent molecule azithromycin into smaller molecules under visible lightirradiation.

A protonated ion peak at m/z 598.59 corresponds to the ceftriaxone sodium compound, resulting from the loss of 3.5 H_2O molecules. The ion peak at m/z 598.59 progressively diminished as other ion peaks emerged with increasing illumination duration, indicating the degradation of the antibiotic. The fragments at m/z 530.59, m/z 413.9, and m/z 396.03 may arise from the loss of a carbonyl group, the cleavage of a C-N bond from the C-8 side chain, and the rupture of a C-N bond from the Ceftriaxone sodium structure, respectively. As deterioration time increases, (m/z 396.03) can decompose into (m/z 112.98), CO_2, and H_2O. The formation of (m/z 243.04) and F (m/z 282) can be attributed to the fracture of β-lactam from the intermediate (m/z 530.59), afterwards, was further decomposed to (m/z 112.98) after C-C bond rupture from C-7 chain, and (m/z 282) could further fragment into (m/z 181) with C-S bond rupture from C-3 chain. (m/z 413.9) can also be converted to (m/z 181). Ultimately, all intermediate products can be decomposed into CO_2, H_2O, and other compounds.

Conclusion
This study fabricated Ag/g-C_3N_4/Fe_3O_4 nanocomposite and optimized PCP for azithromycin and ceftriaxone breakdown in water. The composite's simple structure and high photocatalytic efficiency make it a popular pollutant removal alternative. g-C_3N_4 was synthesized by two-step direct calcination, while the Ag/g-C_3N_4/Fe_3O_4 nanocomposite was made by one-step hydrothermal technique. XRD, DRS, FTIR, FE-SEM, EDS, elemental mapping, TEM, and VSM analytical methods were used to evaluate the produced nanocomposite, achieving the desired properties. The BBD shows that the PCP breaks down azithromycin and ceftriaxone effectively. PCP antibiotic degradation is optimized via the quadratic model. The model's high F-value and low P-value suggest it can explain response value amplification. The absence of fit values, such as the F-value and P-value, supports the model's suitability. PCP degraded azithromycin and ceftriaxone best at pH 5.2, catalyst dosage 0.42 g/L, reaction period 107 min, and starting concentrations of 10 mg/L. The PCP degraded azithromycin 80% and ceftriaxone 91% under these conditions. First-order kinetics correlated well with the results. The PCP's SF coefficient for azithromycin and ceftriaxone degradation was 4.36 and 4.2, respectively. PCP reduced COD and TOC by 65.5% and 52%, respectively, under optimum conditions. Azithromycin and ceftriaxone degradation into intermediates slowed COD and TOC reduction. Increased light intensities boost antibiotic concentration.

Catalysts	Results	Author and reference
Nb-TiO$_2$, Nb-Fe-TiO$_2$	- Successful synthesis with Nb and Fe replacing Ti in TiO$_2$ network. - High photocatalytic activity (up to 70% degradation in 15 min). - Increased specific surface area due to Nb incorporation. - Activation of Fenton photo-oxidation due to Fe^{3+}. - Excellent mechanical and physico-chemical stability.	Giovanina-Iuliana Lupu [81]
Magnetic Graphene Oxide-Zinc Oxide (MZG)	- High degradation efficiency (96.04%) of 50 ppm azithromycin under sunlight in 1 h. - Surface area: 132.9 m^2/g. - Bandgap: 2.8 eV. - Superparamagnetism: Ms 69.78 emu/g. - First-order kinetics (k = 0.0533 min^{-1}). - Good recyclability (only 9% loss after four cycles). - Suitable for industrial applications.	Vineeta Singh[82]
CA-GO-TiO$_2$/PTFE-like thin-film nanocomposite	- Maintained porosity while enhancing thermal and chemical stability. - Predominant C–O bonds in bulk and C–F bonds on PTFE-like coated sides. - Achieved > 80% azithromycin degradation for 2 wt% TiO$_{22}$-GO. - Degradation occurs in two steps, with reaction rates correlated to GO-TiO$_2$ content.	Veronica Satulu[83]
Fe-N-TiO$_2$/PS	- S-VD light modulation achieved highest CEF degradation rate (0.0082 min^{-1}) and 70% TOC removal. - Significant reduction in electric energy consumption (EE/O) compared to literature. - Toxicity of treated CEF solution significantly reduced.	Nicola Morante[84]
CuCoFe$_2$O$_4$@GA/AC	- Nanometer scale (40–50 nm) with high magnetic strength (Ms: 5.38 emu/g) and bandgap of 3.6 eV. - Optimized conditions: pH 5, 60 min irradiation, 0.24 g/L catalyst dose, 5 mg/L ceftriaxone. - Removal efficiency: 94.43% (synthetic) and 62.5% (real samples). - Follows pseudo-first-order and Langmuir–Hinshelwood models. - Superoxide radicals play a major role in degradation. - High recovery capability and chemical stability.	Khadijeh Azarshab[85]
Ag/g-C$_3$N$_4$/Fe$_3$O$_4$	Degradation efficiencies: 83.3 ± 2.1% for azithromycin, 93.3 ± 1.8% for ceftriaxone. COD and TOC reductions: 65.5% and 52%, respectively. Catalyst reusability: less than 13% performance decline after 6 cycles. Dominant role of hydroxyl radicals (OH•) in degradation. Enhanced visible light absorption and electron-hole separation efficiency. Optimal conditions: pH 5.2, 0.42 g/L catalyst dose, 107 min reaction time, 10 mg/L initial antibiotic concentration.	Current study

Table 5. Different catalyst efficiency in the Azithromycin and ceftriaxone degradation.

At 60 mW/cm^2, azithromycin and ceftriaxone were eliminated faster. tert-butanol affected PCP performance most. In contrast, methanol had the least influence. The results show that PO$_4^{3-}$ significantly reduces efficiency. SO$_4^{2-}$ has little effect on PCP performance. The PCP's antimicrobial, COD, and TOC elimination effectiveness was maintained after six cycles. The technique reduced azithromycin and ceftriaxone efficacy by 13% and 12.8%, respectively, after six cycles. PCP EE/O in optimal 17.3 KW/h.m^3 order was calculated. Many peaks have been found, revealing intermediate intermediates from azithromycin and ceftriaxone breakdown.

While this study demonstrates the high efficacy of Ag/g-C$_3$N$_4$/Fe$_3$O$_4$ in antibiotic degradation, several gaps remain that warrant further investigation:

1. Long-Term Stability and Scaling Up: Although the catalyst showed stability over multiple cycles, its long-term application under real wastewater conditions requires further evaluation. The feasibility of large-scale production and industrial applications should also be explored.
2. Toxicity and Byproduct Assessment: The toxicity of the identified intermediates and byproducts has not been fully examined. Future research should assess the potential environmental risks of these degradation products.
3. Mechanistic Insights via Advanced Techniques: The reaction pathways and radical formation mechanisms could be further elucidated using in situ spectroscopy, electron paramagnetic resonance (EPR), or density functional theory (DFT) calculations.
4. Synergistic Effects with Other Water Treatment Methods: The integration of PCP with other advanced oxidation processes (AOPs), membrane filtration, or biological treatments should be investigated to enhance overall degradation efficiency.
5. Effect of Real-World Water Matrices: Further research is needed to evaluate the catalyst's performance in actual wastewater containing diverse contaminants and varying ionic compositions.

Finally, in Table 5, a comparison is made between different catalysts in the removal of the antibiotics azithromycin and ceftriaxone.

Data availability

References

1. Mehralipour, J., Darvishali, S., Bagheri, S. & Kermani, M. Photocatalytic-ozonation process in Oxytetracycline degradation in aqueous solution: composite characterization, optimization, energy consumption, and by-products. *Sci. Rep.* **13**, 11113 (2023).
2. Langbehn, R. K., Michels, C. & Soares, H. M. Antibiotics in wastewater: from its occurrence to the biological removal by environmentally conscious technologies. *Environ. Pollut.* **275**, 116603. https://doi.org/10.1016/j.envpol.2021.116603 (2021).
3. Rawson, T. M. et al. Bacterial and fungal coinfection in individuals with coronavirus: a rapid review to support COVID-19 antimicrobial prescribing. *Clin. Infect. Dis.* **71**, 2459–2468 (2020).
4. Rizvi, S. G. & Ahammad, S. Z. COVID-19 and antimicrobial resistance: A cross-study. *Sci. Total Environ.* **807**, 150873 (2022).
5. Tabrizi, A. M. A., Kakhki, S., Foroughi, M., Khiadani, M. & Mohammadi, M. Z. Azithromycin resistance genes in clinically-isolated Escherichia coli and their relationship with those from wastewater. *J. Taiwan Inst. Chem. Eng.*, **105549** (2024).
6. Karungamye, P., Rugaika, A., Mtei, K. & Machunda, R. A review of methods for removal of ceftriaxone from wastewater. *J. Xenobiot.* **12**, 223–235 (2022).
7. Mehralipour, J., Bagheri, S. & Gholami, M. Synthesis and characterization of rGO/Fe0/Fe3O4/TiO2 nanocomposite and application of photocatalytic process in the decomposition of penicillin G from aqueous. *Heliyon* **9** (2023).
8. Ighnih, H. et al. Synergistic enhancement of pollutant removal from water by using BiOCl/BiOBr heterojunction on clay surface and sunlight irradiation. *J. Water Process. Eng.* **58**, 104766 (2024).
9. Xu, B. et al. Local O2 concentrating boosts the electro-Fenton process for energy-efficient water remediation. *Proc. Natl Acad. Sci.* **121**, e2317702121 (2024).
10. Zhang, Q., Li, W., Peng, J., Xue, L. & He, G. Cold plasma activated Ni 0/ni 2 + interface catalysts for efficient electrocatalytic methane oxidation to low-carbon alcohols. *Green Chem.* **26**, 7091–7100 (2024).
11. Mahmud, F. et al. Antibiotic-contaminated wastewater treatment and remediation by electro-advanced oxidation processes (EAOPs). *Groundw. Sustain. Dev.*, 101181 (2024).
12. Baaloudj, O. et al. Simultaneous removal of antibiotics and inactivation of antibiotic-resistant bacteria by photocatalysis: A review. *J. Water Process. Eng.* **42**, 102089 (2021).
13. Ighnih, H. et al. Sunlight driven photocatalytic degradation of RhB dye using composite of bismuth oxy-bromide kaolinite BiOBr@Kaol: experimental and molecular dynamic simulation studies. *J. Photochem. Photobiol. A.* **445**, 115071 (2023).
14. Wang, Z. et al. Recent advances and insights in designing Zn X Cd1−x S-Based photocatalysts for hydrogen production and synergistic selective oxidation to Value-Added chemical production. *ACS Appl. Mater. Interfaces.* **16**, 48895–48926 (2024).
15. Wang, R., Wang, Z., Yuan, H., Li, C. & Zhu, N. Mechanistic exploration of COVID-19 antiviral drug Ritonavir on anaerobic digestion through experimental validation coupled with metagenomics analysis. *J. Hazard. Mater.* **479**, 135603 (2024).
16. Ighnih, H. et al. Photocatalytic degradation of RhB dye using hybrid nanocomposite BiOCl@ Kaol under sunlight irradiation. *J. Water Process. Eng.* **54**, 103925 (2023).
17. Natarajan, S., Bajaj, H. C. & Tayade, R. J. Recent advances based on the synergetic effect of adsorption for removal of dyes from waste water using photocatalytic process. *J. Environ. Sci.* **65**, 201–222 (2018).
18. Ighnih, H. et al. Efficient removal of hazardous dye from aqueous solutions using magnetic kaolinite nanocomposite: experimental and Monte Carlo simulation studies. *Inorg. Chem. Commun.* **153**, 110886 (2023).
19. Li, X. et al. Recent advances in 3D g-C3N4 composite photocatalysts for photocatalytic water splitting, degradation of pollutants and CO2 reduction. *J. Alloys Compd.* **802**, 196–209 (2019).
20. Wang, H., Wang, B., Bian, Y. & Dai, L. Enhancing photocatalytic activity of graphitic carbon nitride by codoping with P and C for efficient hydrogen generation. *ACS Appl. Mater. Interfaces.* **9**, 21730–21737 (2017).
21. Sharma, J., Kumar, P., Sillanpaa, M., Kumar, D. & Nemiwal, M. Immobilized ionic liquids on Fe3O4 nanoparticles: A potential catalyst for organic synthesis. *Inorg. Chem. Commun.*, 110055 (2022).
22. Ghodsi, S., Esrafili, A., Kalantary, R. R., Gholami, M. & Sobhi, H. R. Synthesis and evaluation of the performance of g-C3N4/Fe3O4/Ag photocatalyst for the efficient removal of Diazinon: kinetic studies. *J. Photochem. Photobiol. A.* **389**, 112279 (2020).
23. Shan, Z. et al. Hollow dodecahedra graphene oxide-cuprous oxide nanocomposites with effective photocatalytic and bactericidal activity. *Front. Chem.* **9**, 755836 (2021).
24. El-Sheekh, M., Alwaleed, E. A., Kassem, W. M. & Saber, H. Optimizing the fucoidan extraction using Box-Behnken design and its potential bioactivity. *Int. J. Biol. Macromol.* **277**, 134490 (2024).
25. Ghodsi, S. et al. Synthesis and application of gC 3 N 4/fe 3 O 4/ag nanocomposite for the efficient photocatalytic inactivation of Escherichia coli and Bacillus subtilis bacteria in aqueous solutions. *AMB Express.* **11**, 1–12 (2021).
26. Duan, J. et al. Facile synthesis of g-C3N4/Fe3O4 nanocomposites for fluorescent detection and removal of Cr(VI). *Microchem. J.* **150**, 104105. https://doi.org/10.1016/j.microc.2019.104105 (2019).
27. Kim, S. P., Choi, M. Y. & Choi, H. C. Photocatalytic activity of SnO2 nanoparticles in methylene blue degradation. *Mater. Res. Bull.* **74**, 85–89. https://doi.org/10.1016/j.materresbull.2015.10.024 (2016).
28. Haque, M. J., Bellah, M. M., Hassan, M. R. & Rahman, S. Synthesis of ZnO nanoparticles by two different methods & comparison of their structural, antibacterial, photocatalytic and optical properties. *Nano Express.* **1**, 010007 (2020).
29. Mehralipour, J., Bagheri, S. & Gholami, M. Synthesis and characterization of rGO/Fe0/Fe3O4/TiO2 nanocomposite and application of photocatalytic process in the decomposition of penicillin G from aqueous. *Heliyon* (2023).
30. Mehralipour, J., Vakili, B., Aria, E. A., Kermani, M. & Ghobadi, N. Synthesis and characterization of Bi2S3@ NH2-MIL125 (Ti) and survey the sono-catalytic ozonation process's efficiency in the degradation of Tocilizumab from aqueous. *Inorg. Chem. Commun.*, 113118 (2024).
31. Zhang, H. et al. Degradation of ibuprofen by the UV/chlorine/TiO2 process: kinetics, influencing factor simulation, energy consumption, toxicity and byproducts. *Chem. Eng. J.* **450**, 137849 (2022).
32. Bagheri, S., Esrafili, A., Kermani, M., Mehralipour, J. & Gholami, M. Performance evaluation of a novel rGO-Fe0/Fe3O4-PEI nanocomposite for lead and cadmium removal from aqueous solutions. *J. Mol. Liq.* **320**, 114422 (2020).
33. Nosaka, Y. & Nosaka, A. Y. Langmuir–Hinshelwood and light-intensity dependence analyses of photocatalytic oxidation rates by two-dimensional-ladder kinetic simulation. *J. Phys. Chem. C.* **122**, 28748–28756 (2018).
34. Al-Hakkani, M. F. A rapid, developed and validated RP-HPLC method for determination of Azithromycin. *SN Appl. Sci.* **1**, 222 (2019).
35. Patel, K. Y., Dedania, Z. R., Dedania, R. R. & Patel, U. QbD approach to HPLC method development and validation of ceftriaxone sodium. *Fut. J. Pharm. Sci.* **7**, 1–10 (2021).
36. Guo, S. et al. in *IOP Conference Series: Materials Science and Engineering.* 012091 (IOP Publishing).
37. Hafeez, H. Y. et al. Synergistic utilization of magnetic rGO/NiFe2O4-g-C3N4 S-Scheme heterostructure photocatalyst with enhanced charge carrier separation and transfer: a highly stable and robust photocatalyst for efficient solar fuel (hydrogen) generation. *Ceram. Int.* **49**, 5269–5278 (2023).
38. Kumar, S., Kumar, B., Baruah, A. & Shanker, V. Synthesis of magnetically separable and recyclable g-C3N4–Fe3O4 hybrid nanocomposites with enhanced photocatalytic performance under visible-light irradiation. *J. Phys. Chem. C.* **117**, 26135–26143 (2013).
39. Zhu, Z. et al. Construction of high-dispersed Ag/Fe3O4/g-C3N4 photocatalyst by selective photo-deposition and improved photocatalytic activity. *Appl. Catal. B.* **182**, 115–122. https://doi.org/10.1016/j.apcatb.2015.09.029 (2016).
40. Habibi-Yangjeh, A. & Mousavi, M. Deposition of CuWO4 nanoparticles over g-C3N4/Fe3O4 nanocomposite: novel magnetic photocatalysts with drastically enhanced performance under visible-light. *Adv. Powder Technol.* **29**, 1379–1392 (2018).

21

41. Wen, J., Xie, J., Chen, X. & Li, X. A review on g-C3N4-based photocatalysts. *Appl. Surf. Sci.* **391**, 72–123 (2017).
42. Xu, R. & Peng, Y. Preparation of magnetic g-C3N4/Fe3O4 composite and its application in the separation of catechol from water. *Materials* **12**, 2844 (2019).
43. Brindha, B. et al. Dynamic Ag-mediated electron transfer confined ZnO nanorods for boosted photocatalytic bacterial disinfection. *J. Clean. Prod.* **451**, 141908 (2024).
44. Danmaliki, G. I., Saleh, T. A. & Shamsuddeen, A. A. Response surface methodology optimization of adsorptive desulfurization on nickel/activated carbon. *Chem. Eng. J.* **313**, 993–1003. https://doi.org/10.1016/j.cej.2016.10.141 (2017). https://doi.org/http://dx.
45. Arslan, A., Topkaya, E., Bingöl, D. & Veli, S. Removal of anionic surfactant sodium Dodecyl sulfate from aqueous solutions by O3/UV/H2O2 advanced oxidation process: process optimization with response surface methodology approach. *Sustain. Environ. Res.* **28**, 65–71 (2018).
46. Pugachevskii, M. A., Mamontov, V. A., Syuy, A. V. & Kuzmenko, A. P. Effect of pH on antioxidant properties of ablated CeO2 nanoparticles in photocatalytic process. *J. Ind. Eng. Chem.* **106**, 74–76 (2022).
47. Jabbar, Z. H. & Graimed, B. H. Recent developments in industrial organic degradation via semiconductor heterojunctions and the parameters affecting the photocatalytic process: A review study. *J. Water Process. Eng.* **47**, 102671 (2022).
48. Barjasteh-Askari, F. et al. Photocatalytic removal of Diazinon from aqueous solutions: a quantitative systematic review. *Environ. Sci. Pollut. Res.* **29**, 26113–26130 (2022).
49. Sattari, M., Farhadian, M., Nazar, A. R. S. & Moghadam, M. Enhancement of phenol degradation, using of novel Z-scheme Bi2WO6/C3N4/TiO2 composite: catalyst and operational parameters optimization. *J. Photochem. Photobiol. A.* **431**, 114065 (2022).
50. Yeganeh, M., Charkhloo, E., Sobhi, H. R., Esrafili, A. & Gholami, M. Photocatalytic processes associated with degradation of pesticides in aqueous solutions: systematic review and meta-analysis. *Chem. Eng. J.* **428**, 130081. https://doi.org/10.1016/j.cej.2021.130081 (2022).
51. Al-Hasani, H., Al-Sabahi, J., Al-Ghafri, B., Al-Hajri, R. & Al-Abri, M. Effect of water quality in photocatalytic degradation of phenol using zinc oxide nanorods under visible light irradiation. *J. Water Process. Eng.* **49**, 103121 (2022).
52. Steffy, J. et al. Facet engineering in Au nanoparticles buried in Cu2O nanocubes for enhanced catalytic degradation of Rhodamine B and larvicidal application. *Sustain. Mater. Technol.* **43**, e01185 (2025).
53. Mehrabadi, Z. & Faghihian, H. Clinoptilolite modified with TiO2 for simultaneous elimination of two herbicides; 2,4-D and MCPA by UV and sunlight-assisted photocatalytic degradation. *Mater. Res. Bull.* **119**, 110569. https://doi.org/10.1016/j.materresbull.2019.110569 (2019).
54. Chavoshan, S., Khodadadi, M. & Nasseh, N. Photocatalytic degradation of penicillin G from simulated wastewater using the UV/ZnO process: isotherm and kinetic study. *J. Environ. Health Sci. Eng.* **18**, 107–117 (2020).
55. Sneha, Y., Yashas, S. R., Thinley, T., Prabagar Jijoe, S. & Puttaiah Shivaraju, H. Photocatalytic degradation of Lomefloxacin antibiotics using hydrothermally synthesized magnesium titanate under visible light-driven energy sources. *Environ. Sci. Pollut. Res.* **29**, 67969–67980 (2022).
56. Arslan, H., Eskikaya, O., Bilici, Z., Dizge, N. & Balakrishnan, D. Comparison of cr (VI) adsorption and photocatalytic reduction efficiency using Leonardite powder. *Chemosphere* **300**, 134492 (2022).
57. Saadati, F., Keramati, N. & Ghazi, M. M. Influence of parameters on the photocatalytic degradation of Tetracycline in wastewater: a review. *Crit. Rev. Environ. Sci. Technol.* **46**, 757–782 (2016).
58. Liang, Y. et al. Black titanium dioxide nanomaterials for photocatalytic removal of pollutants: A review. *J. Mater. Sci. Technol.* **112**, 239–262 (2022).
59. Moradeeya, P. G., Kumar, M. A., Sharma, A. & Basha, S. Conductive polymer layered semiconductor for degradation of Triclopyr acid and 2, 4-dichlorophenoxyacetic acid from aqueous stream using coalesce adsorption-photocatalysis technique. *Chemosphere* **298**, 134360 (2022).
60. Jia, Z. M., Zhao, Y. R. & Shi, J. N. Adsorption kinetics of the photocatalytic reaction of nano-TiO2 cement-based materials: a review. *Constr. Build. Mater.* **370**, 130462 (2023).
61. Yu, Y. et al. Synergistic adsorption-photocatalytic degradation of different antibiotics in seawater by a porous g-C3N4/calcined-LDH and its application in synthetic mariculture wastewater. *J. Hazard. Mater.* **416**, 126183. https://doi.org/10.1016/j.jhazmat.2021.126183 (2021).
62. Rathi, A., Basu, S. & Barman, S. Efficient eradication of antibiotic and dye by C-dots@zeolite nanocomposites: performance evaluation, and degraded products analysis. *Chemosphere* **298**, 134260. https://doi.org/10.1016/j.chemosphere.2022.134260 (2022).
63. Yang, C. et al. Photocatalytic PVDF ultrafiltration membrane blended with visible-light responsive Fe (III)-TiO2 catalyst: degradation kinetics, catalytic performance and reusability. *Chem. Eng. J.* **417**, 129340 (2021).
64. Balakrishnan, A. & Chinthala, M. Comprehensive review on advanced reusability of g-C3N4 based photocatalysts for the removal of organic pollutants. *Chemosphere* **297**, 134190. https://doi.org/10.1016/j.chemosphere.2022.134190 (2022).
65. Deba, S. A. H., Wols, B. A., Yntema, D. R. & Lammertink, R. G. Photocatalytic ceramic membrane: effect of the illumination intensity and distribution. *J. Photochem. Photobiol., A.* **437**, 114469 (2023).
66. Moradi, M. et al. Visible-light-driven photocatalytic inactivation of Escherichia coli by titanium dioxide anchored on natural pyrite. *Inorg. Chem. Commun.* **144**, 109913. https://doi.org/10.1016/j.inoche.2022.109913 (2022).
67. Rapti, I., Kosma, C., Albanis, T. & Konstantinou, I. Solar photocatalytic degradation of inherent pharmaceutical residues in real hospital WWTP effluents using titanium dioxide on a CPC pilot scale reactor. *Catal. Today* (2022).
68. Balakrishnan, A., Appunni, S. & Gopalram, K. Immobilized TiO2/chitosan beads for photocatalytic degradation of 2,4-dichlorophenoxyacetic acid. *Int. J. Biol. Macromol.* **161**, 282–291. https://doi.org/10.1016/j.ijbiomac.2020.05.204 (2020).
69. Makama, A. B. et al. Influence of parameters and radical scavengers on the visible-light-induced degradation of Ciprofloxacin in ZnO/SnS2 nanocomposite suspension: identification of transformation products. *Chemosphere* **253**, 126689. https://doi.org/10.1016/j.chemosphere.2020.126689 (2020).
70. Yang, R. et al. One-step Preparation (3D/2D/2D) BiVO4/FeVO4@ rGO heterojunction composite photocatalyst for the removal of Tetracycline and hexavalent chromium ions in water. *Chem. Eng. J.* **390**, 124522 (2020).
71. Shyamala, R. & Gomathi Devi, L. Reduced graphene oxide/SnO2 nanocomposites for the photocatalytic degradation of Rhodamine B: preparation, characterization, photosensitization, vectorial charge transfer mechanism and identification of reaction intermediates. *Chem. Phys. Lett.* **748**, 137385. https://doi.org/10.1016/j.cplett.2020.137385 (2020).
72. Elbadawy, H. A., Elhusseiny, A. F., Hussein, S. M. & Sadik, W. A. Sustainable and energy-efficient photocatalytic degradation of textile dye assisted by ecofriendly synthesized silver nanoparticles. *Sci. Rep.* **13**, 2302 (2023).
73. Mehralipour, J., Vakili, B., Aria, E. A., Kermani, M. & Ghobadi, N. Synthesis and characterization of Bi2S3@ NH2-MIL125 (Ti) and survey the sono-catalytic ozonation process's efficiency in the degradation of Tocilizumab from aqueous. *Inorg. Chem. Commun.* **169**, 113118 (2024).
74. Shafeeyan, M. S. Application of photocatalytic and Fenton processes for the degradation of toxic pollutants from pulp and paper industry effluents. *Water Resour. Ind.*, **100260** (2024).
75. Zhang, X. et al. Efficiently enhanced visible-light photocatalytic activity by in situ deposition of Ag@ AgBr on g-C3N4/Fe3O4 magnetic heterogeneous materials. *Sep. Purif. Technol.* **254**, 117596 (2021).
76. Zhang, X. et al. High-efficiency removal of Tetracycline by carbon-bridge-doped g-C3N4/Fe3O4 magnetic heterogeneous catalyst through photo-Fenton process. *J. Hazard. Mater.* **418**, 126333 (2021).

22

77. Mousavi, M., Habibi-Yangjeh, A. & Seifzadeh, D. Novel ternary g-C3N4/Fe3O4/MnWO4 nanocomposites: synthesis, characterization, and visible-light photocatalytic performance for environmental purposes. *J. Mater. Sci. Technol.* **34**, 1638–1651 (2018).

78. Sabariselvan, L. et al. Engineering sulfur defect rich Vs-ZnS with sulfur vacancies modulated charge transfer for high performance photocatalytic degradation of Levofloxacin. *J. Water Process. Eng.* **69**, 106761. https://doi.org/10.1016/j.jwpe.2024.106761 (2025).

79. Sre, V. V. et al. Unveiling the enhanced photocatalytic degradation of metronidazole over green-synthesized Ag@ZnCdS QDs Schottky heterojunction: pathway, toxicity evaluation and mechanistic insights. *J. Water Process. Eng.* **62**, 105325. https://doi.org/10.1016/j.jwpe.2024.105325 (2024).

80. Naraginti, S., Yu, Y. Y., Fang, Z. & Yong, Y. C. Visible light degradation of macrolide antibiotic Azithromycin by novel ZrO2/Ag@TiO2 Nanorod composite: transformation pathways and toxicity evaluation. *Process Saf. Environ. Prot.* **125**, 39–49. https://doi.org/10.1016/j.psep.2019.02.031 (2019).

81. Lupu, G. I. et al. Photocatalytic degradation of Azithromycin formulation in aqueous solution by doped titanium dioxide/fiberglass-rubberized silicone photocatalytic membrane. *Sustain. Environ. Res.* **33**, 36 (2023).

82. Singh, V. & Samanta, S. K. Magnetic graphene oxide-zinc oxide nanocomposite for enhanced photocatalytic degradation of Azithromycin under normal sunlight. *J. Environ. Manag.* **370**, 122571. https://doi.org/10.1016/j.jenvman.2024.122571 (2024).

83. Satulu, V. et al. Robust CA-GO-TiO2/PTFE photocatalytic membranes for the degradation of the Azithromycin formulation from wastewaters. *Polymers* **16**, 1368 (2024).

84. Morante, N. et al. Influence of visible light leds modulation techniques on photocatalytic degradation of ceftriaxone in a flat plate reactor. *Chem. Eng. J.* **482**, 149175. https://doi.org/10.1016/j.cej.2024.149175 (2024).

85. Azarshab, K., Hashemi, M., Nasiri, A. & Khodabakhshi, A. Synthesis and characterization of CuCoFe2O4@ GA/AC as a bio-based matrix magnetic nano-heterogeneous photocatalyst for ceftriaxone degradation from aqueous media. *Appl. Water Sci.* **14**, 197 (2024).

Acknowledgements

Author contributions

Amirali Emadi Khyave: conceived and designed the experiments, analyzed and interpreted the data, materials, contributed reagents, materials, analysis tools or data, wrote the paper.Asghar Davood: performed the experiments, materials, contributed reagents, materials, wrote the paper.Amirhossein Mahvi: performed the experiments, materials, contributed reagents, materials, wrote the paper.Lida Salimi: performed the experiments, materials, contributed reagents, materials, wrote the paper.Roya Mafigholami: conceived and designed the experiments, analyzed and interpreted the data, wrote the paper.

Funding

Declarations

Competing interests

The authors declare no competing interests.

Ethics approval

1398.595.

Additional information

Supplementary Information The online version contains supplementary material available at https://doi.org/10.1038/s41598-025-00149-5.

Correspondence and requests for materials should be addressed to R.M.

Reprints and permissions information is available at www.nature.com/reprints.

Publisher's note Springer Nature remains neutral with regard to jurisdictional claims in published maps and institutional affiliations.